

AD \_\_\_\_\_

Award Number: DAMD17-02-1-0081

TITLE: Compact Positron Tomograph for Prostate Imaging

PRINCIPAL INVESTIGATOR: Jennifer S. Huber, Ph.D.

CONTRACTING ORGANIZATION: Ernest Orlando Lawrence Berkeley  
National Laboratory  
Berkeley, CA 94701

REPORT DATE: January 2005

TYPE OF REPORT: Final

PREPARED FOR: U.S. Army Medical Research and Materiel Command  
Fort Detrick, Maryland 21702-5012

DISTRIBUTION STATEMENT: Approved for Public Release;  
Distribution Unlimited

The views, opinions and/or findings contained in this report are those of the author(s) and should not be construed as an official Department of the Army position, policy or decision unless so designated by other documentation.

**REPORT DOCUMENTATION PAGE**Form Approved  
OMB No. 074-0188

Public reporting burden for this collection of information is estimated to average 1 hour per response, including the time for reviewing instructions, searching existing data sources, gathering and maintaining the data needed, and completing and reviewing this collection of information. Send comments regarding this burden estimate or any other aspect of this collection of information, including suggestions for reducing this burden to Washington Headquarters Services, Directorate for Information Operations and Reports, 1215 Jefferson Davis Highway, Suite 1204, Arlington, VA 22202-4302, and to the Office of Management and Budget, Paperwork Reduction Project (0704-0188), Washington, DC 20503

<b>1. AGENCY USE ONLY</b> (Leave blank)		<b>2. REPORT DATE</b> January 2005	<b>3. REPORT TYPE AND DATES COVERED</b> Final (10 Dec 2001 - 9 Dec 2004)	
<b>4. TITLE AND SUBTITLE</b>  Compact Positron Tomograph for Prostate Imaging			<b>5. FUNDING NUMBERS</b> DAMD17-02-1-0081	
<b>6. AUTHOR(S)</b>  Jennifer S. Huber, Ph.D.				
<b>7. PERFORMING ORGANIZATION NAME(S) AND ADDRESS(ES)</b> Ernest Orlando Lawrence Berkeley National Laboratory Berkeley, CA 94701  E-Mail: jshuber@lbl.gov			<b>8. PERFORMING ORGANIZATION REPORT NUMBER</b>	
<b>9. SPONSORING / MONITORING AGENCY NAME(S) AND ADDRESS(ES)</b> U.S. Army Medical Research and Materiel Command Fort Detrick, Maryland 21702-5012			<b>10. SPONSORING / MONITORING AGENCY REPORT NUMBER</b>	
<b>11. SUPPLEMENTARY NOTES</b>  Original contains color plates: ALL DTIC reproductions will be in black and white.				
<b>12a. DISTRIBUTION / AVAILABILITY STATEMENT</b> Approved for Public Release; Distribution Unlimited				<b>12b. DISTRIBUTION CODE</b>
<b>13. ABSTRACT (Maximum 200 Words)</b> <p>The goal of this project is to construct a functioning compact positron tomograph, whose geometry is optimized for detecting prostate tumors with molecular tracers such as [<sup>11</sup>C]choline (carbon-11 choline), in order to confirm the presence, absence or progression of prostate cancer. The camera consist of two banks of detectors mounted in a gantry. The bottom bank is fixed below the patient bed, and the top bank moves upward for patient access and downward for maximum sensitivity.</p> <p>The camera design was optimized, and extensive simulations were used to evaluate the expected camera performance. The camera was constructed. An iterative reconstruction algorithm was developed and tested with real data. Initial camera performance characterization was completed by imaging several phantoms with the system. Reconstructed images of extended and point source phantoms, using the completed camera in 3D-mode operation, demonstrate the feasibility of imaging prostate tumors with good spatial resolution and image contrast. The reconstruction algorithm will be fully optimized, the septa will be built and installed, and all NEMA phantom imaging will be completed by April, 2005.</p>				
<b>14. SUBJECT TERMS</b>  positron emission tomography, prostate				<b>15. NUMBER OF PAGES</b> 36
				<b>16. PRICE CODE</b>
<b>17. SECURITY CLASSIFICATION OF REPORT</b> Unclassified	<b>18. SECURITY CLASSIFICATION OF THIS PAGE</b> Unclassified	<b>19. SECURITY CLASSIFICATION OF ABSTRACT</b> Unclassified	<b>20. LIMITATION OF ABSTRACT</b> Unlimited	

NSN 7540-01-280-5500

Standard Form 298 (Rev. 2-89)  
Prescribed by ANSI Std. Z39-18  
298-102

## Table of Contents

Cover.....	1
SF 298.....	2
Table of Contents.....	3
Introduction.....	4
Body.....	4
Key Research Accomplishments.....	8
Reportable Outcomes.....	8
Conclusions.....	9
References.....	9
Appendices.....	9

## 4. INTRODUCTION

The goal of this project is to construct a functioning compact positron tomograph, whose geometry is optimized for detecting prostate tumors with molecular tracers such as [ $^{11}\text{C}$ ]choline (carbon-11 choline), to confirm the presence, absence or progression of prostate cancer. Compared with a conventional positron emission tomography (PET) camera, the proposed tomograph has (1) the same spatial resolution in the region of the prostate; (2) improved detection efficiency; and (3) significantly lower cost, which would increase clinical availability. See Figure 1 for a sketch of the positron tomograph, consisting of detector banks, patient and patient bed. See Appendix 1 for three-dimensional color drawings that show the gantry details. See Figure 2 for photographs of a partially-assembled and fully-assembled camera. See Appendices 3-6 for technical papers presented at scientific meetings.

## 5. BODY OF THE PROGRESS REPORT

Below are the list of tasks as proposed in our original Statement of Work. A summary of our progress and current status for each sub-task follows.

### **Task 1** Design two external curved detector banks; Months 1-10:

- a) Determine optimal detector bank geometry based on simulations and calculations.
- b) Design shielding.
- c) Design gantry.
- d) Design phantom bed.

### **Task 2** Construct the camera; Months 3-26:

- a) Construct gantry.
- b) Purchase and test CTI ECAT HR+ PET detector modules.
- c) Configure detector modules into two detector banks.
- d) Construct and test event processing, coincidence processing, and readout electronics.
- e) Configure system with phantom bed.

### **Task 3** Develop iterative reconstruction algorithms; Months 2-31:

- a) Develop iterative algorithms using Monte Carlo generated data.
- b) Optimize algorithms using real data.

### **Task 4** Characterize camera performance with phantoms; Months 27-36.

#### **Task 1(a): Determine optimal detector bank geometry**

Based on our computer simulations and calculations, we have optimized and finalized the design of the PET camera [1, 2]. Figure 1 shows the transaxial and sagittal views of the camera. The bottom bank is fixed below the patient bed, and the top bank moves upward for patient access and downward for maximum sensitivity. Each bank consists of two axial rows of 20 CTI ECAT HR+ detector modules, forming two arcs with a minor axis of 45 cm and a major axis of 70 cm. Our original proposal allowed for only a single axial row, but patient alignment will be significantly easier with greater axial coverage; we negotiated with CPS Innovations to receive the CTI ECAT HR+ detector modules at below cost (to afford the second axial row). Individual detector modules are angled to point towards the camera center in order to optimize resolution at the center near the

prostate at the price of some resolution degradation at the edges. Both detector banks can be tilted to image the prostate while minimizing attenuation (*i.e.*, above the buttocks and below the stomach, see Figure 1b), but the gantry allows zero tilt for thin patients.

#### Task 1(b): Design shielding

The camera design includes shielding (see Figure 1b). Tungsten septa extend beyond the scintillator crystals to reduce background events from random coincidences and from photons that Compton scatter in the patient. Lead shields are also used on the ends to reduce activity from outside the field of view. Our original septa design consisted of tungsten septa with an uniform length of 5 cm placed between each scintillator crystal, which was based on geometric calculations with reference to the design of current clinical whole-body scanners. However, we used Monte Carlo simulations to further investigate several novel septa designs [3], in addition to considering manufacturing issues and cost. As a result, we chose a design with a single tungsten septa (2.4 mm thick, with a ~5 cm length that varies to match the lead shields) placed axially between detector modules, as shown in Figure 1b.

#### Task 1(c): Design gantry

The gantry and electronics housing design has been completed. Figure 2 shows photographs of the camera with many of the gantry and electronics housing details, and Appendix 1 shows a 3D drawing with more gantry details. The upper bank is mounted on a main aluminum back-plate in order to control the vertical motion using a hand-crank, allowing upward movement for patient access and downward to maximize sensitivity. A second hand-crank is used to adjust the overall tilt of both upper and lower banks. The near end of Figure 2b (and Appendix 2) shows the electronics housing; see Appendices 3 and 5 for further electronics details. The electronics used for another project is similar to this system [4-5]. The  $\pm 5V$  and high-voltage power supplies are mounted on the left-side of the gantry in Figure 2b (visible in Appendix 1b).

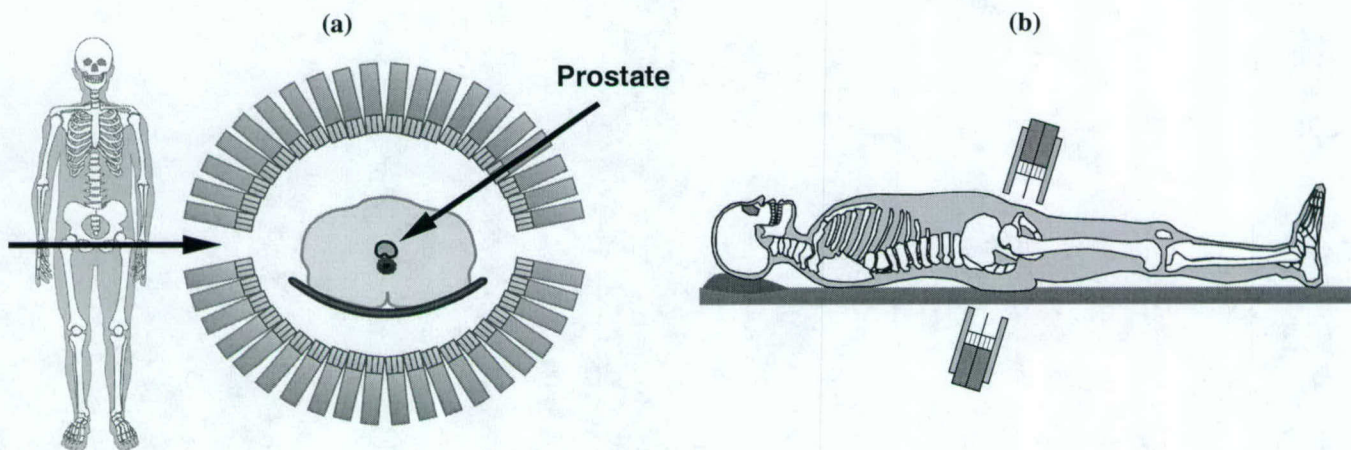


**Figure 1:** Positron tomograph for prostate imaging. (a) Drawing of a transaxial view through prostate, showing the patient centered between two detector banks (shielding not shown). The individual detector modules are angled to point towards the prostate. (b) Drawing of the sagittal view with shielding shown. The bottom arc is fixed below the patient bed, whereas the top arc adjusts vertically for patient access and compactness. Both detector banks are tilted and positioned as close as possible to the prostate, which improves sensitivity and minimizes attenuation.

#### Task 1(d): Design phantom bed

Our proposal was limited to the design, construction and characterization (using phantoms) of a compact prostate imaging system. Since human studies are beyond the

scope of this proposal, we were only required to design a simple phantom bed for this proposal. However, we were able to modify and use an existing patient bed instead.

**Task 2(a): Construct gantry**

Construction of the gantry, electronics housing, cabling, and power supplies is complete, as shown in Figure 2b and Appendix 2.

**Task 2(b): Purchase and test CTI ECAT HR+ PET detector modules**

We acquired all CTI ECAT HR+ detector modules and electronics boards from CPS Innovations at a reduced cost, allowing us to build the PET camera with two axial rows of detector modules rather than the single ring originally proposed. All detector modules have been tested and demonstrated to work properly.

**Task 2(c): Configure detector modules into two detector banks**

Figure 2 shows photographs of the partially-assembled and fully-assembled camera. All 80 detector modules have been configured into two detector banks.

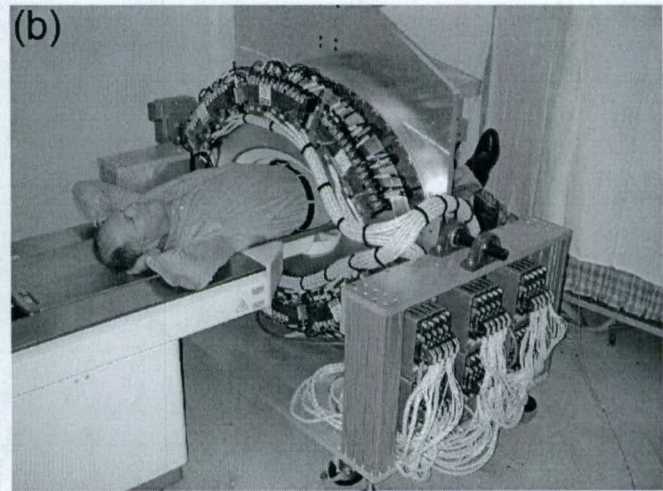
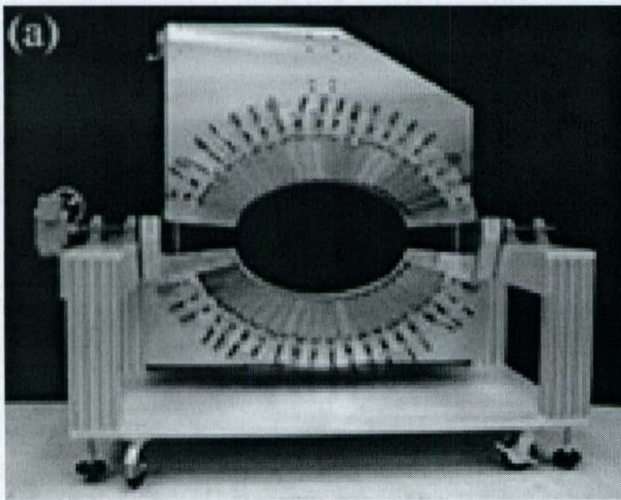


**Figure 2:.** (a) Photograph of the partially-assembled camera with a single axial row of detector modules visible. The detector modules are individually angled to point towards the center of the camera. (b) Photograph of the gantry fully loaded with electronics and shielding. A patient will lie on his back on the patient bed and the detector banks will be positioned close to the patient for improved sensitivity.

**Task 2(d): Construct and test event processing, coincidence processing, and readout electronics**

We have tested and modified the CPS Innovations electronics and data acquisition software for our system, as well as designed and constructed the required conversion boards (for the Analog Subsection boards). We have tested the event processing, coincidence processing and readout electronics using real (single and coincidence) data. We have developed software for our system, including software to calibrate our detector modules and readout electronics. The camera is fully-calibrated and complete.

**Task 2(e): Configure system with phantom bed**

We have configured the PET camera with a patient bed, as evidenced by Figure 2b and Appendix 2. The only missing component is the septa, which is still under construction due to an unexpected delay in purchasing the tungsten material.

### Task 3(a): Develop iterative algorithms using Monte Carlo generated data

The reconstruction algorithm has been developed. We did a significant amount of simulation work to evaluate the expected camera performance as well as to optimize the camera design. We determined the size of the region with high spatial resolution within our PET camera, showing that there will be optimal resolution in the 10 cm diameter central region near the prostate for a wide range of patient sizes [2]. We addressed the issue of irregular and incomplete sampling due to the side gaps between the detector banks [1-2].

Reconstructions were performed with an iterative maximum likelihood technique that assumes statistical noise representing 745 kcounts/slice, a tumor activity concentration that is two times the background activity concentration, 30% scatter fraction, and 20% randoms fraction. The reconstructions were then post-filtered with a very conservative Gaussian function of  $\sigma = 1$  pixel = 2 mm. We demonstrated that we can reconstruct nearly artifact-free images, as well as detect and differentiate partial and whole prostate tumors, using Monte Carlo data equivalent to a 6-minute scan after a 10 mCi radiopharmaceutical injection. The expected camera performance is discussed in further detail in Appendix 5. We explored the necessary data corrections, such as attenuation correction and normalization.

### Task 3(b): Optimize algorithms using real data

Optimization of the reconstruction algorithms using real data is nearly complete. The normalization procedure still needs to be finalized. Further details are discussed in Appendices 3 and 6.

### Task 4: Characterize camera performance with phantoms

Characterization of camera performance, following the current NEMA performance measurements, is in progress. Figures 3 and 4 show reconstructed images of two different phantoms. Reconstructed images of extended and point source phantoms demonstrate the feasibility of imaging prostate tumors with good spatial resolution and image contrast. All NEMA phantom imaging should be completed by April, 2005.

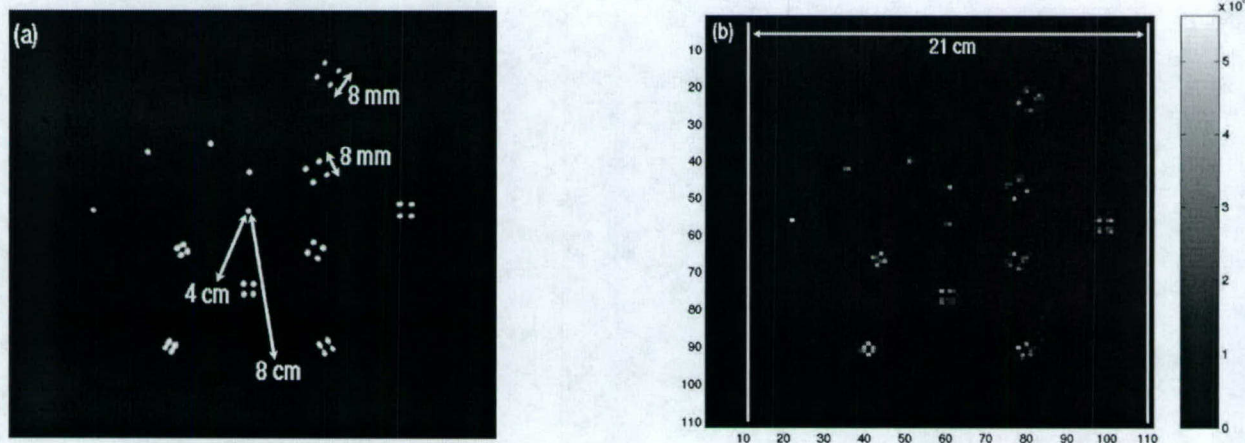


**Figure 3:** (a) Drawing of a cylindrical phantom (21 cm diameter, 5 cm axial) with 37 point sources. The single point sources are 2, 4, 6, and 8 cm from the central point. Clusters of 4 point sources are placed radially at 4 and 8 cm from the central point. The 4 point sources in each cluster are spaced 8, 6, 5, and 4 mm apart (clockwise from the 8 mm labeled clusters). (b) Reconstructed image of the phantom using an iterative penalized ML algorithm, demonstrating that we can resolve point sources that are separated by 4 mm when placed at a diameter of 8 cm and 16 cm (*i.e.*, a larger region than the prostate bed). Phantom was filled with  $^{18}\text{F}$  at an initial activity of 0.6 mCi and imaged for 2 minutes. The central point was placed in the center of the camera. Image represents 10 Mcounts. Axes are labeled in pixels (2 mm).

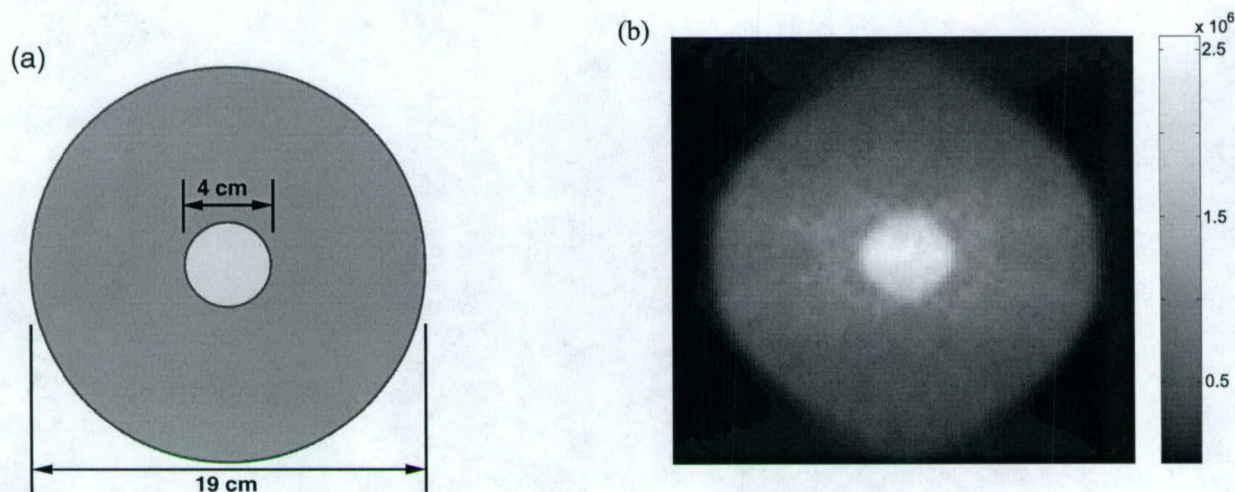


**Figure 4:** (a) A concentric-cylinder phantom with three times higher activity density in the central cylinder than the outer cylinder. (b) Preliminary reconstructed image of the phantom using an iterative penalized ML algorithm. Initial total  $^{18}\text{F}$  activity density was  $0.25 \mu\text{Ci/ml}$  and the imaging time was 3 minutes. Image represents 20 Mcounts.

## 6. KEY RESEARCH ACCOMPLISHMENTS

- The camera design was optimized and completed.
- Extensive simulations were used to evaluate the expected camera performance.
- Construction of the camera was completed.
- An iterative reconstruction algorithm was developed and tested with real data.
- Initial camera performance characterization was completed by imaging several phantoms with the system.

## 7. REPORTABLE OUTCOMES

J. S. Huber, J. Qi, S. E. Derenzo, W. W. Moses, et al., "The Development of a Compact Positron Tomograph for Prostate Imaging," *LBNL-50790*, 2002. Oral presentation at the 2002 Institute of Electrical and Electronics Engineers (IEEE) Nuclear Science Symposium and Medical Imaging Conference, Norfolk, VA, USA.

J. Qi, J. S. Huber, R. H. Huesman, W. W. Moses, S. E. Derenzo, and T. F. Budinger, "Septa Design for a Prostate-Specific PET Camera," *IEEE Trans Nucl Sci*, NS-51, In Press, 2004. Oral presentation at the 2003 IEEE Nuclear Science Symposium and Medical Imaging Conference, Portland, OR, USA.

J. S. Huber, W. S. Choong, W. W. Moses, J. Qi, J. Hu, D. Wilson, S. Oh, R. H. Huesman, S. E. Derenzo, and T. F. Budinger, "Initial Results of a Positron Tomograph for Prostate Imaging," *IEEE Trans Nucl Sci*, NS-51, Submitted, 2004. Presentation at the 2004 IEEE Nuclear Science Symposium and Medical Imaging Conference, Rome, Italy.

J. Hu, J. Qi, J. S. Huber, W. W. Moses, and R. H. Huesman, "MAP Image Reconstruction for Arbitrary Geometry PET Systems with Application to a Prostate-Specific Scanner," Fully 3D Image Reconstruction Meeting on Radiology and Nuclear Medicine, Submitted, Salt Lake City, Utah, USA, 2005.

NIH R21 grant proposal (in response to PA-04-045) submitted February 1, 2005.

## 8. CONCLUSIONS

Task 1 has been completed. Design of the detector bank geometry, electronics, gantry, electronics housing and bed was optimized. The septa design was improved.

Task 2 has been completed for 3D-mode camera operation; construction of the septa must be completed before operating in 2D-mode. The gantry components were fabricated and assembled. All detector modules and electronics were acquired and tested. Software for data acquisition and calibration was developed. The system was fully assembled.

Task 3 is nearly complete. Extensive simulations were used to evaluate the expected camera performance. An iterative reconstruction algorithm was developed and tested with real data. Optimization of the reconstruction algorithm is nearly complete.

Task 4 is in progress. Using phantom imaging, we have demonstrated the feasibility of imaging prostate tumors with good spatial resolution and image contrast.

## 9. REFERENCES

- [1] J. S. Huber, S. E. Derenzo, J. Qi, et al., "Conceptual Design of a Compact Positron Tomograph for Prostate Imaging," *IEEE Trans Nucl Sci*, vol. NS-48, pp. 1506-1511, 2001.
- [2] J. S. Huber, J. Qi, S. E. Derenzo, et al., "The Development of a Compact Positron Tomograph for Prostate Imaging," *LBNL-50790*, 2002.
- [3] J. Qi, J. S. Huber, R. H. Huesman, et al., "Septa Design for a Prostate-Specific PET Camera," *IEEE Trans Nucl Sci*, NS-51, In Press, 2004.
- [4] W. W. Moses, J. W. Young, K. Baker, et al., "The Electronics System for the LBNL Positron Emission Mammography (PEM) Camera," *IEEE Trans Nucl Sci*, vol. NS-48, pp. 632-636, 2001.
- [5] J. S. Huber, W. S. Choong, W. W. Moses, J. Qi, J. Hu, D. Wilson, S. Oh, R. H. Huesman, S. E. Derenzo, and T. F. Budinger, "Initial Results of a Positron Tomograph for Prostate Imaging" *IEEE Trans Nucl Sci*, NS-51, Submitted, 2004.
- [6] J. Hu, J. Qi, J. S. Huber, W. W. Moses, and R. H. Huesman, "MAP Image Reconstruction for Arbitrary Geometry PET Systems with Application to a Prostate-Specific Scanner," Submitted to Fully 3D Image Reconstruction Meeting on Radiology and Nuclear Medicine, 2005.

## 10. APPENDICES

**Appendix 1:** 3D color drawings of the prostate PET camera with gantry details.

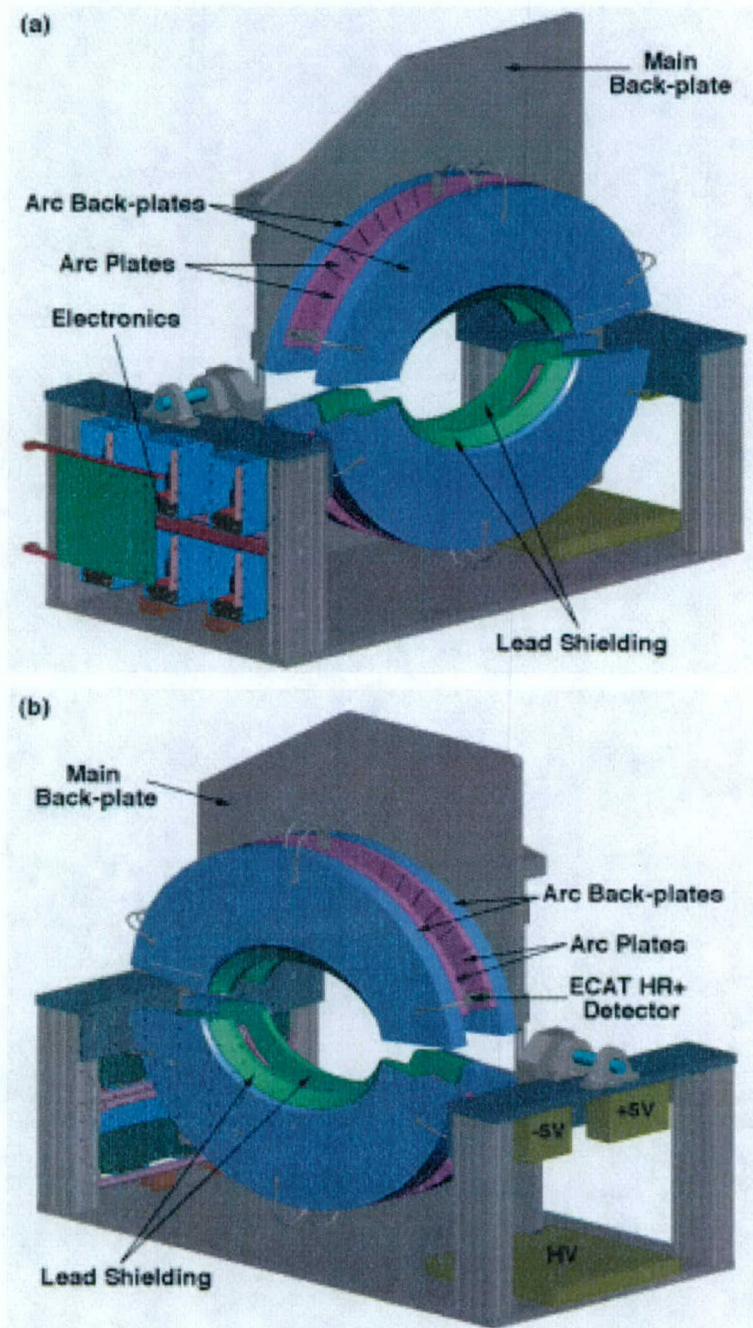
**Appendix 2:** Color photograph of the fully-assembled PET camera.

**Appendix 3:** J. S. Huber, W. S. Choong, W. W. Moses, et al., "Initial Results of a Positron Tomograph for Prostate Imaging," *IEEE Trans Nucl Sci*, NS-51, Submitted, 2004.

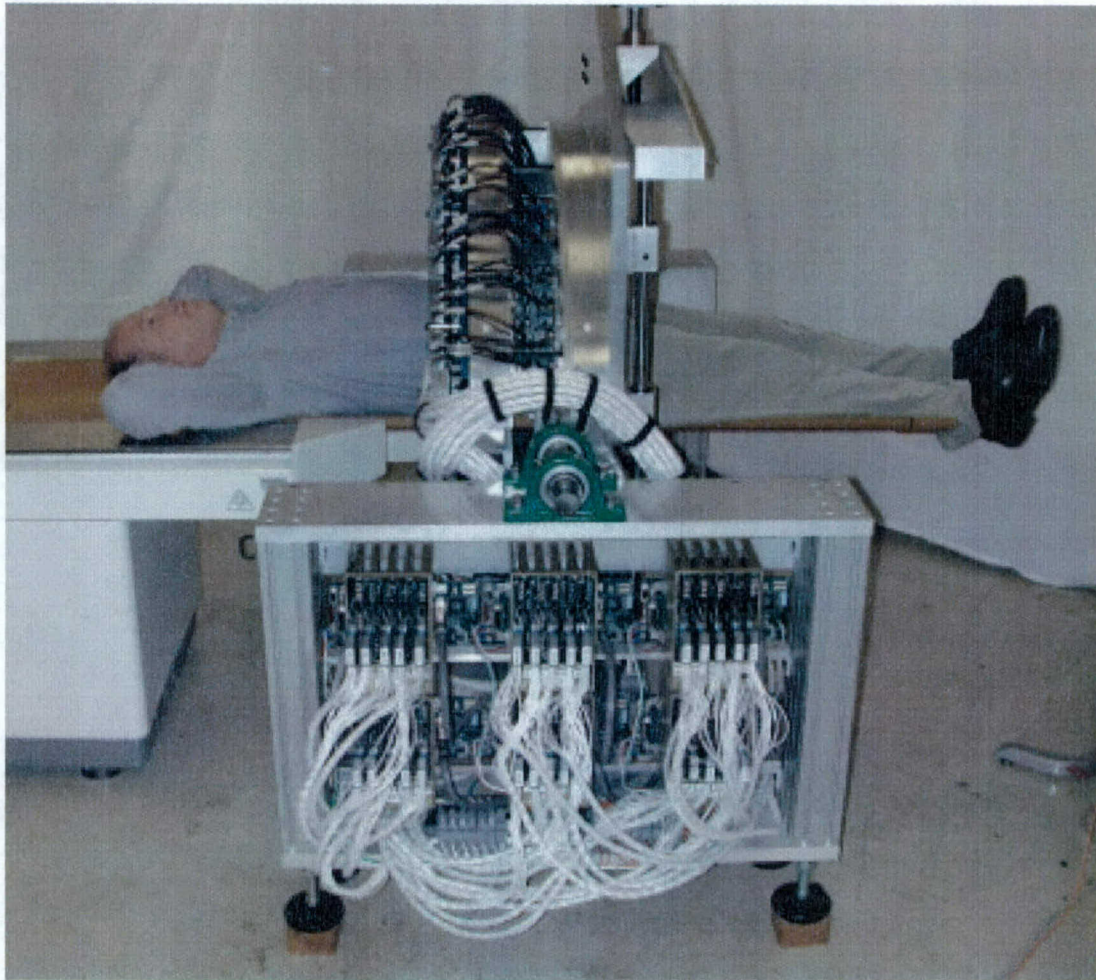
**Appendix 4:** J. Qi, J. S. Huber, R. H. Huesman, et al., "Septa Design for a Prostate-Specific PET Camera," *IEEE Trans Nucl Sci*, NS-51, In Press, 2004.

**Appendix 5:** J. S. Huber, J. Qi, S. E. Derenzo, et al., "The Development of a Compact Positron Tomograph for Prostate Imaging," *LBNL-50790*, 2002.

**Appendix 6:** J. Hu, J. Qi, J. S. Huber, et al., "MAP Image Reconstruction for Arbitrary Geometry PET Systems with Application to a Prostate-Specific Scanner," Submitted to the Fully 3D Image Reconstruction Meeting on Radiology and Nuclear Medicine, 2005.



**Appendix 1:** 3-D color drawings of the prostate PET camera with some gantry details. Only a few detector modules are shown in place. The arc plates are mounted on thicker aluminum arc back-plates that also hold the lead shielding. The arc plates (pink), arc back-plates (blue) and lead shielding (green) are symmetrical since there are two axial rows of detector modules. The upper bank is mounted on a main aluminum back-plate in order to control the vertical motion using a hand-crank. A second hand-crank is used to adjust the overall tilt of both upper and lower banks. Most of the cabling is not shown, as well as the patient bed. (a) The near end of the drawing shows the electronics. The six Detector Head Interface boards are mounted horizontally to the housings that hold their corresponding Analog Subsection boards. The Coincidence Processor board is mounted on the cabinet door. (b) The near end of the drawing shows the power supplies.



**Appendix 2:** Photograph of the fully-assembled PET camera.

# Initial Results of a Positron Tomograph for Prostate Imaging

J. S. Huber, *Member, IEEE*, W.S. Choong, *Member, IEEE*, W. W. Moses, *Senior Member, IEEE*, J. Qi, *Member, IEEE*, J. Hu, *Member, IEEE*, G.C. Wang, *Member, IEEE*, D. Wilson, S. Oh, R. H. Huesman, *Fellow, IEEE*, S. E. Derenzo, *Fellow, IEEE*, and T. F. Budinger, *Member, IEEE*

**Abstract**—We present the status and initial images of a positron tomograph for prostate imaging that centers a patient between a pair of external curved detector banks (ellipse: 45 cm minor, 70 cm major axis). The distance between detector banks adjusts to allow patient access and to position the detectors as closely as possible for maximum sensitivity with patients of various sizes. Each bank is composed of two axial rows of 20 CTI PET Systems HR+ block detectors for a total of 80 modules in the camera. Compared to an ECAT HR PET system operating in 3D mode, our camera uses about one-quarter the number of detectors and has approximately the same sensitivity for a central point source, because our detectors are close to the patient. The individual detectors are angled in the plane to point towards the prostate to minimize resolution degradation in that region. The detectors are read out by modified CTI data acquisition electronics. We have completed construction of the gantry and electronics, have developed detector calibration and data acquisition software, and are taking coincidence data. We demonstrate that we can clearly visualize a "prostate" in a simple phantom. Reconstructed images of two phantoms are shown.

## 1. INTRODUCTION

WE present the development of a positron tomograph optimized to image the prostate. This instrument images radiopharmaceuticals that specifically localize in the prostate to confirm the presence, absence or progression of disease. It has approximately four times fewer detectors than an ECAT HR or HR+ PET scanner, which will reduce the cost and potentially increase clinical availability.

Prostate cancer has a prevalence and diagnostic rate similar to breast cancer, with 230,000 new cases diagnosed in the United States each year and one man in 6 diagnosed during his lifetime. Prostate cancer suspicion is typically based on an elevated prostate-specific antigen (PSA) level or a suspicious mass found during a digital rectal exam. Treatment decision is based mainly on biopsy confirmation

of prostate cancer. Typical treatment options include prostatectomy, external beam irradiation, brachytherapy (interstitial implantation of radioactive seeds), androgen ablation (hormone) therapy, or "watchful waiting." A major problem with prostatic cancer therapy is the question of where to biopsy, when to treat, or whether to treat at all. This is particularly problematic in the case of an increased PSA level with non-diagnostic repeated biopsies or after a prostatectomy. A new imaging technology for sensitive detection of prostate cancer is needed to confirm initial diagnosis, guide biopsy and help guide treatment decisions. In addition, a new method is needed to assess response shortly after a treatment intervention.

In order to help meet these needs, we have built a PET camera optimized to image the prostate. Functional PET imaging will help detect malignant tumors in the prostate and/or prostate bed as a follow-up for an elevated PSA level, as well as possibly help determine tumor "aggressiveness" based on metabolic uptake levels. Although not optimized to detect distant metastatic disease, this PET camera should also image local spread beyond the prostate bed to help guide treatment decisions such as whether a narrow or wide irradiation treatment field is needed.

Promising PET radiopharmaceuticals have recently demonstrated outstanding results in the sensitive detection of prostate cancer, inspiring a new interest in using PET for prostate cancer imaging. Consistent with the evidence of increased pool size of choline in prostate cancer [1, 2], Hara and co-workers find that: [ $^{11}\text{C}$ ]choline clears the blood faster than FDG; its uptake in prostate tumors is significantly higher than in normal and surrounding tissues [3, 4], providing excellent tumor/normal contrast; and bladder accumulation is minimal if the correct time course is chosen [5] which is a major advantage over FDG. Therefore, [ $^{11}\text{C}$ ]choline is an attractive PET tracer for imaging primary and metastatic tumors of the prostate and potentially for other regions of the body [6-10]. Other  $^{11}\text{C}$  radiopharmaceuticals are also under investigation for prostate cancer PET imaging, including [ $^{11}\text{C}$ ]acetate and [ $^{11}\text{C}$ ]methionine.

$^{18}\text{F}$  imaging has the advantage of a longer half-life, which increases clinical utility because an on-site cyclotron facility would not be necessary (as it would for  $^{11}\text{C}$  imaging). Although many groups have shown that PET imaging with [ $^{18}\text{F}$ ]fluorodeoxyglucose (FDG) is not a good technique for prostate cancer diagnosis, there are several other  $^{18}\text{F}$

Manuscript received December 1, 2004. This work was supported in part by the Director, Office of Science, Office of Biological and Environmental Research, Medical Science Division of the U.S. Department of Energy under Contract No. DE-AC03-76SF00098, in part by Department of Defense grant number DAMD17-02-1-0081, and in part by National Institute for Biomedical Imaging and Bioengineering grant number R01 EB 00194.

J. S. Huber, W.S. Choong, W. W. Moses, J. Hu, D. Wilson, S. Oh, R. H. Huesman and S.E. Derenzo are with the Lawrence Berkeley National Laboratory, Mailstop 55-121, 1 Cyclotron Road, Berkeley, CA 94720 USA (telephone: 510-486-6445, e-mail: jshuber@lbl.gov). J. Qi is with the Department of Biomedical Engineering, University of California, Davis, CA 95616 USA (telephone: 530-754-6142, email: qi@ucdavis.edu).

radiopharmaceuticals currently under investigation including [ $^{18}\text{F}$ ]fluorocholine (FCH) [11, 12]. PET images using [ $^{18}\text{F}$ ]fluorocholine demonstrate high standardized uptake values (*e.g.*, SUV of 8), indicating that FCH is well localized in the prostate cancer and can be imaged with good resolution if short scan times (~five minutes) are used to avoid bladder background.

## II. CAMERA DESIGN

### A. Overview

These new prostate tracers motivated us to build a low cost PET camera optimized to image the prostate. Coincidence imaging of positron emitters is achieved using a pair of external curved detector banks, one placed above and one below the patient. Fig. 1 shows the transaxial and sagittal views of the camera. The bottom bank is fixed below the patient bed, and the top bank moves upward for patient access and downward for maximum sensitivity. Each bank consists of two axial rows of 20 CTI ECAT HR+ block detectors (80 detectors total in the camera), forming two arcs with a minor axis of 45 cm and major axis of 70 cm. Our prostate camera has about one-fourth the number of detectors as an EXACT HR or HR+ because: (a) the patient is not fully encircled in 2D, (b) an elliptical shape is used instead of a circular one, and (c) the axial coverage is only 8 cm. However, since the average distance to the detectors is approximately one-half that of a conventional PET system, we expect to achieve improved detection efficiency at a lower cost.

Individual detector modules are angled to point towards the camera center near the prostate location in order to reduce penetration effects (in the detector) for annihilation photons originating in the prostate. This geometry increases resolution selectively in the region of the prostate and is a unique feature for a non-circular camera geometry. Annihilation photons from other parts of the field of view (FOV) will suffer increased penetration effects, but these regions are less important. Both detector banks can be tilted to image the prostate while minimizing attenuation (*i.e.*, above the buttocks and below the stomach, see Fig. 1b), but the gantry allows zero tilt for thin patients. A patient of average size is not fully encircled in 2D, which results in irregular and incomplete sampling due to the side gaps. Despite this incomplete sampling, we are able to reconstruct nearly artifact free images in the region of interest by using an iterative reconstruction algorithm [13].

The camera design also includes shielding [13], as shown in Fig. 1b. Inter-module septa extend 5 cm beyond the scintillator crystals to reduce background events from random coincidences and from photons that Compton scatter in the patient [14]. These septa have not yet been built, so we have operated in septa-less 3D mode for the data presented here. Lead shields are used on the ends to reduce activity from outside the field of view.

### B. Electronics

Our camera uses modified commercial components in a novel geometry. We use 80 CTI ECAT HR+ block detectors that are three attenuation lengths thick for good detection efficiency with narrow detector elements (*i.e.*, 8 x 8 arrays of 4.5 x 4.5 x 30 mm<sup>3</sup> BGO crystals) to achieve good spatial resolution. We use modified front end, coincidence, and readout electronics developed by CTI for the HRRT brain imaging PET camera, as shown in Fig. 2. Since we are creating a non-standard camera with HR+ and HRRT components, a custom conversion board reroutes PMT signals to electronics channel inputs. Events are detected and assigned an arrival time, the crystal of interaction is identified, energy qualification is performed, and a digital word is formed using 28 CTI HRRT Analog Subsection boards. The output signals from the Analog Subsection boards are then multiplexed by six custom Detector Head Interface (DHI) boards, which are based on the CTI HRRT DHI design but each services a maximum of 15 (rather than 117) detector modules. We use six DHI boards to allow coincidences between detector modules within the same bank and plane. A CTI Coincidence Processor identifies singles events in the different DHI boards that are in coincidence, and the output is sent to a Pentium-based computer system for reconstruction and display.

### C. Gantry

The PET camera is complete except for the construction of the septa. Fig. 3 shows a photograph of the camera with the lead shielding on one side removed and a single row of detector modules visible. Each detector module points toward the center of the camera, as discussed in Section IIA. The upper bank is mounted onto an aluminum back-plate whose vertical motion is controlled using a hand-crank, allowing upward movement for patient access and downward motion to maximize sensitivity. A second hand-crank is used to adjust the overall tilt of both upper and lower banks. The readout electronics are mounted on the right housing (within the Unistrut frame visible on the right in Fig. 3b). The six DHI boards are mounted horizontally to the housing that holds their corresponding Analog Subsection boards. The Coincidence Processor board is mounted onto the cabinet door for compactness. The  $\pm 5\text{V}$  and high voltage power supplies are mounted on the left housing.

## III. PERFORMANCE

### A. Sensitivity and Count Rate

Coincidence event rates were measured by scanning a 1.5 mm diameter 120  $\mu\text{Ci}$   $^{68}\text{Ge}$  point source along the central axis of the patient port in 3 mm steps. A 270 keV energy threshold was used for all measurements with a 22 nsec coincidence timing window. Figure 4 shows the system sensitivity as a function of axial position. The peak absolute sensitivity is 1010 cps/ $\mu\text{Ci}$  (2.7%) in 3D mode. This is equivalent to the peak absolute sensitivity of the EXACT HR in 3D mode and approximately 8 times higher than the

EXACT HR in 2D mode, even though our camera has one-quarter as many detectors.

The count rate as a function of activity density was measured using a 19 cm inner diameter by 19 cm long cylindrical phantom filled with  $^{18}\text{F}$  and centered in the camera. Data were collected in 3D mode for 10 seconds every 20 minutes over a time span of 12 half-lives. Figure 5a shows the count rate as a function of activity density for total, prompt, random and true+scatter coincident events. The maximum total count rate was 1.2 Mhz at an 1.5  $\mu\text{Ci/ml}$  activity density. Figure 5b shows the count rate at only the lower activity density corresponding to a standard clinical range. The trues+scatter events cross the randoms at 0.23  $\mu\text{Ci/ml}$ .

### B. Reconstruction Algorithm

We have developed a penalized maximum likelihood reconstruction algorithm for the prostate camera. The reconstruction software is designed to be very flexible in modeling arbitrary scanner geometry. Forward and back projections at each iteration are calculated using the exact position and orientation of each detector block without any rebinning. The crystal penetration effect is modeled using a geometric calculation technique similar to that presented in [15] for a positron emission mammography scanner. The attenuation correction factors are calculated based on the measured phantom geometry and a uniform attenuation coefficient of 0.095/cm. A pixel size of 2 mm is used. We estimate and subtract the random background using the standard delayed window technique. The reconstruction algorithm [13], including the normalization procedure, is not yet final so we present only preliminary results.

### C. Reconstructed Images

Rectangular planar phantoms are used for normalization. Coincident data are acquired with a 27" x 4" x 0.375" planar phantom centered between the detector banks (*i.e.*, placed horizontally in Fig 3b), in order to correct for coincident events that occur between detector banks. Coincident data are acquired separately with a 10.6" x 4" x 0.375" planar phantom placed perpendicular to the 27" phantom (*i.e.*, placed vertically in Fig 3b), in order to correct for coincident events that occur within the same detector bank.

Figure 6a shows a 37-point phantom. Single point sources are placed 2, 4, 6 and 8 cm from the central point. Clusters of 4 point sources are placed radially at 4 and 8 cm from the central point, and the points in each cluster are spaced 8, 6, 5 and 4 mm apart. Figure 6b shows the preliminary reconstructed image of this 37-point phantom when filled with  $^{18}\text{F}$  at an initial activity of 0.6 mCi and imaged for two minutes. Increased blurring is seen for point sources placed further from the center. This blurring is primarily caused by missing projections, because the crystal penetration effect is modeled in the projection matrix. Minimal blurring is seen in the 10 cm diameter central region. We are able to resolve point sources that are separated by 4 mm when placed at a diameter of 8 cm and 16 cm.

Figure 7a shows a concentric-cylinder phantom with three times higher activity density in the inner cylinder than the outer cylinder. Figure 7b shows the reconstructed image of this phantom when filled with  $^{18}\text{F}$  at an initial total activity density of 0.4  $\mu\text{Ci/ml}$  and imaged for four minutes. We can clearly visualize a "prostate" in a simple phantom, when the "prostate" has a three times higher activity density than the "body." Imperfect normalization factors result in some noticeable streak artifacts. We expect the results to improve once detector efficiency drifts have been minimized. Artifacts at the top and bottom of the image are due to incomplete sampling from the detector bank gaps.

## IV. DISCUSSION

PET radiopharmaceuticals have recently demonstrated promising results in the sensitive detection of prostate cancer. Initially we plan to image using [ $^{11}\text{C}$ ]choline. In the future, this camera can be used to evaluate new prostate cancer radiopharmaceuticals. The high sensitivity of this new design can achieve clinical imaging wherein short duration scans are needed to avoid bladder background accumulation of tracers.

Accurate patient positioning is critical due to the limited (8 cm) axial extent of the camera. The prostate is visible in ultrasound images acquired with an external or trans-rectal transducer, and we plan to use these images to position the patient bed.

Finally, it is difficult to identify features other than the prostate and the bladder in the PET images. Local anatomic information is highly desirable to determine the location of the disease within the prostate, as well as to determine whether the disease has spread to the prostate bed. This information could be obtained with dual modality imaging. X-ray CT provides excellent images of the abdomen, but the cost is relatively high. Ultrasound imaging with a trans-rectal probe provides reasonable detail in the region of the prostate and the cost of an ultrasound unit is significantly less than that of a CT unit. We plan to explore adding co-registered ultrasound imaging capability, including the use of dual imaging for *in situ* guided biopsy.

## V. CONCLUSION

Promising new PET tracers for prostate cancer, such as [ $^{11}\text{C}$ ]choline and [ $^{11}\text{C}$ ]acetate, have motivated us to build a PET camera optimized for prostate imaging. Reconstructed images of extended and point source phantoms demonstrate the feasibility of imaging prostate tumors with good spatial resolution and image contrast at low cost relative to commercial whole body PET scanners. The same sensitivity as ECAT HR in 3D mode is achieved using only one-quarter the number of detector modules and an axial length of 8 cm. Before the camera is ready for patient imaging, we still need to build the septa, automate the calibration procedure, finalize the reconstruction algorithm, and characterize the camera following NEMA performance measurements.

## VI. ACKNOWLEDGMENT

We thank Dr. Ronald Nutt from CPS Innovations for providing detectors and electronics. This work was supported in part by the Director, Office of Science, Office of Biological and Environmental Research, Medical Science Division of the U.S. Department of Energy under Contract No. DE-AC03-76SF00098, in part by Department of Defense grant number DAMD17-02-1-0081, and in part by National Institute for Biomedical Imaging and Bioengineering grant number R01 EB 00194. Reference to a company or product name does not imply approval or recommendation by the University of California or the U.S. Department of Energy to the exclusion of others that may be suitable.

## VII. REFERENCES

1. J. Kurhanewicz, D. B. Vigneron, H. Hricak, et al., "Three-dimensional H-1 MR spectroscopic imaging of the in situ human prostate with high (0.24-0.7-cm<sup>3</sup>) spatial resolution," *Radiology*, vol. 198, pp. 795-805, 1996.
2. J. Kurhanewicz, D. B. Vigneron, R. G. Males, et al., "The Prostate: Magnetic Resonance Imaging and Spectroscopy: Present and Future," in *Radiologic Clinics of North America*, H. Hricak and P. R. Carroll, Eds. New York, New York: W. B. Saunders Co., 2000, pp. 115-138.
3. T. Hara, N. Kosaka, N. Shinoura, et al., "PET imaging of brain tumor with [methyl-C11]choline," *J Nucl Med*, vol. 38, pp. 842-7, 1997.
4. N. Shinoura, M. Nishijima, T. Hara, et al., "Brain tumors: detection with C-11 choline PET," *Radiology*, vol. 202, pp. 497-503, 1997.
5. T. Hara, N. Kosaka, and H. Kishi, "PET imaging of prostate cancer using carbon-11-choline," *J Nucl Med*, vol. 39, pp. 990-5, 1998.
6. T. Hara, N. Kosaka, T. Kondo, et al., "Imaging of brain tumor, lung cancer, esophagus cancer, colon cancer, prostate cancer, and bladder cancer with [C-11]choline," *J Nucl Med*, vol. 38 (suppl), pp. 250P (abstract), 1997.
7. T. Hara, K. Inagaki, N. Kosaka, et al., "Sensitive detection of mediastinal lymph node metastasis of lung cancer with 11C-choline PET," *J Nucl Med*, vol. 41, pp. 1507-13, 2000.
8. I. J. Jong, T. H. Que, J. Pruijm, et al., "Imaging of bladder cancer using carbon-11 choline positron emission tomography," *J. Nucl. Med.*, vol. 41 (5 Suppl), pp. 74, 2000.
9. J. Kotzerke, J. U. Prang, B. Neumaier, et al., "Carbon-11 choline positron emission tomography (PET) of prostate cancer -- first clinical experience," *J. Nucl. Med.*, vol. 41 (5 Suppl), pp. 74, 2000.
10. J. Kotzerke, J. Prang, B. Neumaier, et al., "Experience with carbon-11 choline positron emission tomography in prostate carcinoma," *Eur J Nucl Med*, vol. 27, pp. 1415-9, 2000.
11. T. R. Degrad, R. E. Coleman, S. W. Baldwin, et al., "Fluorine-18 fluorocholine (FCH) as an oncological PET tracer: evaluation in murine prostate cancer xenograft model," *J. Nucl. Med.*, vol. 41 (5 Suppl), pp. 231, 2000.
12. T. R. Degrad, R. E. Coleman, S. Wang, et al., "Synthesis and Evaluation of F18-labeled Choline as an Oncologic Tracer for Positron Emission Tomography: Initial Findings in Prostate Cancer," *Cancer Research*, vol. 61(1), pp. 110-117, 2001.
13. J. S. Huber, S. E. Derenzo, J. Qi, et al., "Conceptual Design of a Compact Positron Tomograph for Prostate Imaging," *IEEE Trans Nucl Sci*, vol. NS-48, pp. 1506-1511, 2001.
14. J. Qi, J. S. Huber, R. H. Huesman, et al., "Septa Design for a Prostate Specific PET Camera," *IEEE Trans Nucl Sci*, vol. NS-51, pp. In Press, 2004.
15. R. H. Huesman, G. J. Klein, W. W. Moses, et al., "List mode maximum likelihood reconstruction applied to positron emission mammography with irregular sampling," *IEEE Trans Med Imag*, vol. 19, pp. 532-537, 2000.

## Figures:

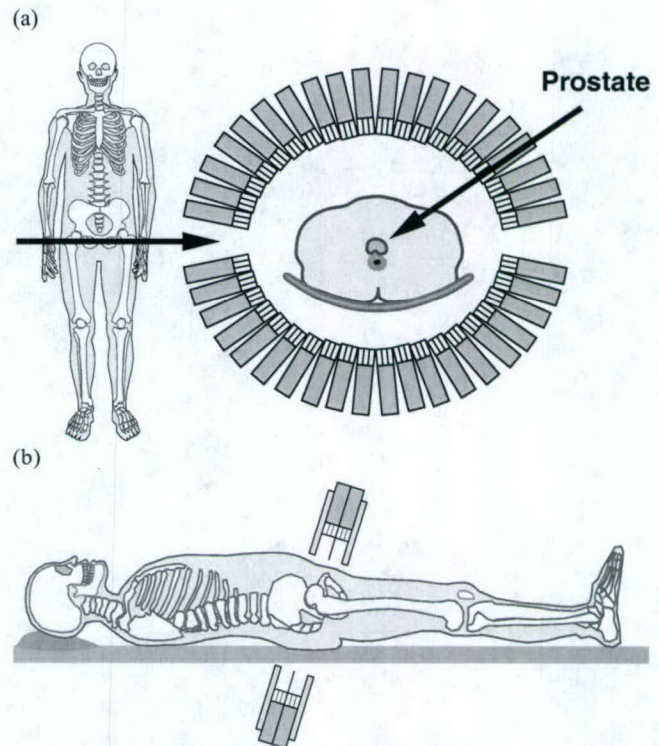


Fig. 1: Positron tomograph for prostate imaging. (a) Drawing of a transaxial view through prostate, showing the patient centered between two detector banks. The individual detector modules are angled to point towards the prostate. No shielding is shown. (b) Drawing of the sagittal view. The bottom arc is fixed below the patient bed, whereas the top arc adjusts vertically for patient access and compactness. Both detector banks are tilted and positioned as close as possible to the prostate, which improves sensitivity and minimizes attenuation. The septa and lead shielding are shown.

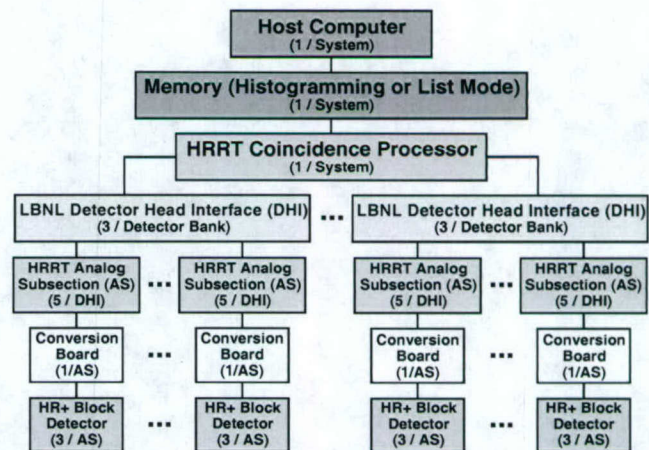


Fig. 2: Diagram of the complete data collection chain, showing the custom LBNL and CTI components and their inter-relations. The camera will use 80 CTI ECAT HR+ block detectors, 28 LBNL conversion boards, 28 CTI HRRT Analog Subsection boards, 6 LBNL custom Detector Head Interface boards, 1 CTI Coincidence Processor and a PC.

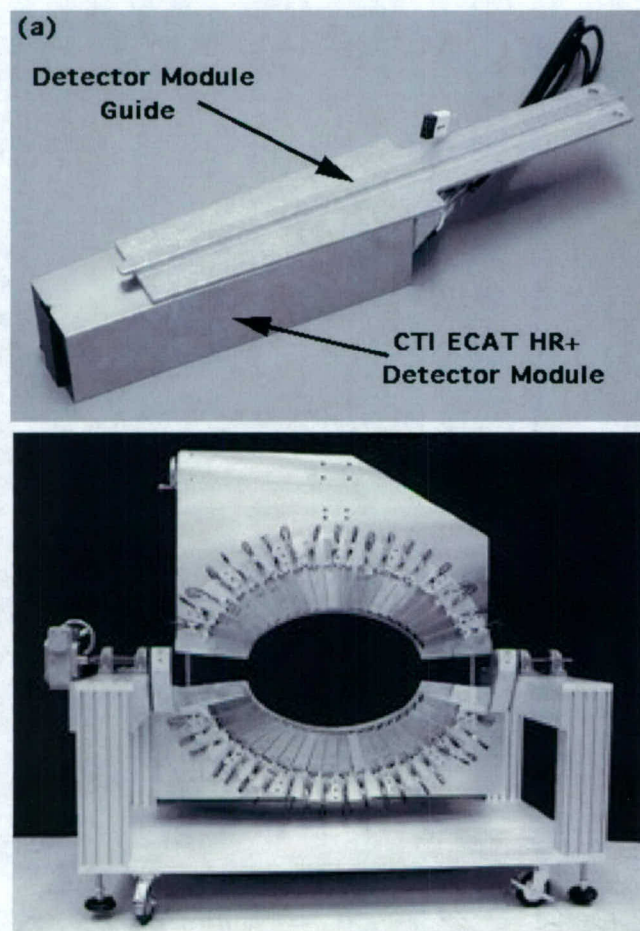


Fig. 3: (a) CTI ECAT HR+ detector module with an aluminum guide epoxied along its midline (that is used to position and secure the module). (b) Photograph of the partially-assembled camera with a single axial row of detector modules visible. The detector modules are individually angled to point towards the center of the camera. The gantry is now complete and fully loaded with electronics and shielding. The camera is complete expect for the septa.

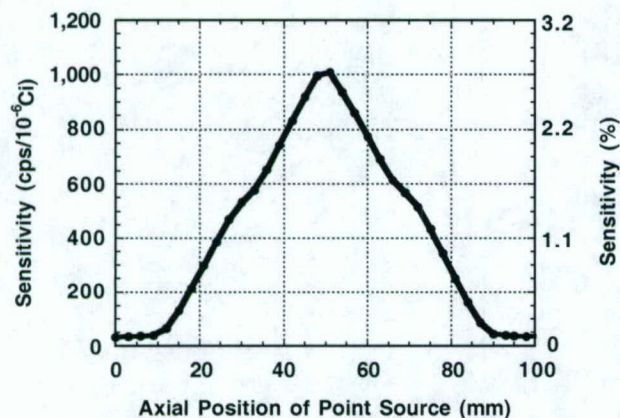


Fig. 4: System sensitivity as a function of axial position, using an 120  $\mu\text{Ci}$   $^{68}\text{Ge}$  point source. Peak absolute sensitivity in the center of the field of view is 1010 cps/ $\mu\text{Ci}$  (2.7%) in 3D mode, which is the same as an EXACT HR in 3D mode but with one-quarter as many detector modules. Data was collected using a 270 keV energy threshold.

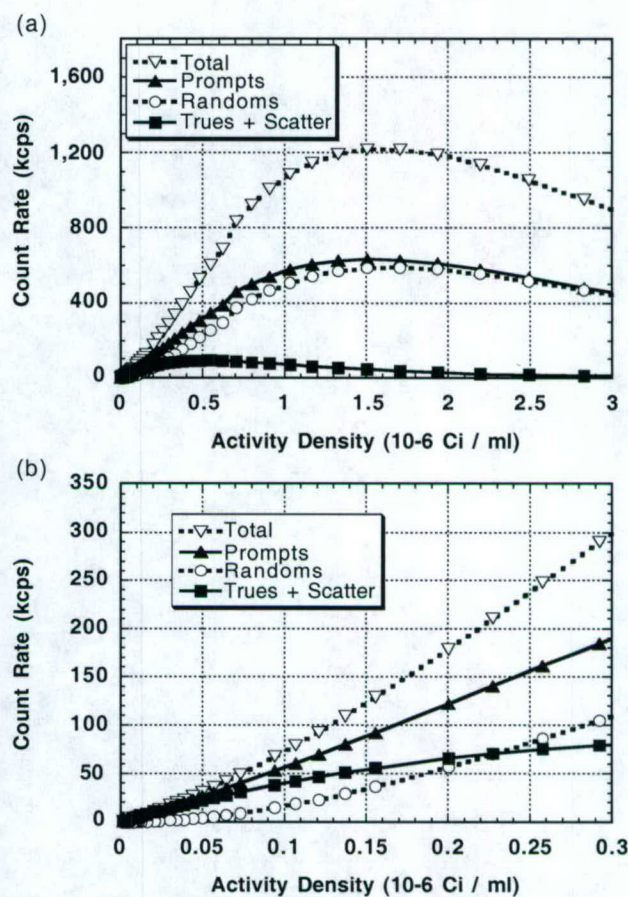


Fig. 5: Count rate as a function of activity density for total, prompt, random and true+scatter coincident events acquired with a cylindrical phantom (19 cm ID, 19 cm length) filled with  $^{18}\text{F}$  and centered in the camera. Plots show two different ranges of activity density.

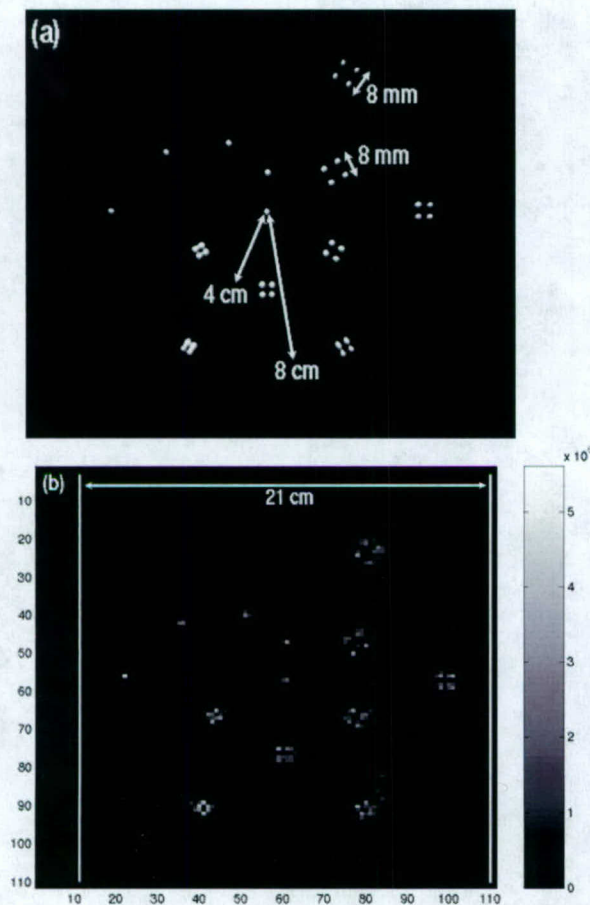


Fig. 6: (a) Drawing of a cylindrical phantom (21 cm diameter, 5 cm axial) with 37 point sources. The single point sources are 2, 4, 6, and 8 cm from the central point. Clusters of 4 point sources are placed radially at 4 and 8 cm from the central point. The 4 point sources in each cluster are spaced 8, 6, 5, and 4 mm apart (clockwise from the 8 mm labeled clusters). (b) Reconstructed image of the phantom using a preliminary iterative penalized ML algorithm. Phantom was filled with  $^{18}\text{F}$  at an initial activity of 0.6 mCi and imaged for 2 minutes. The central point was placed in the center of the camera. Image represents 10 Mcounts. Axes are labeled in pixels (2 mm).

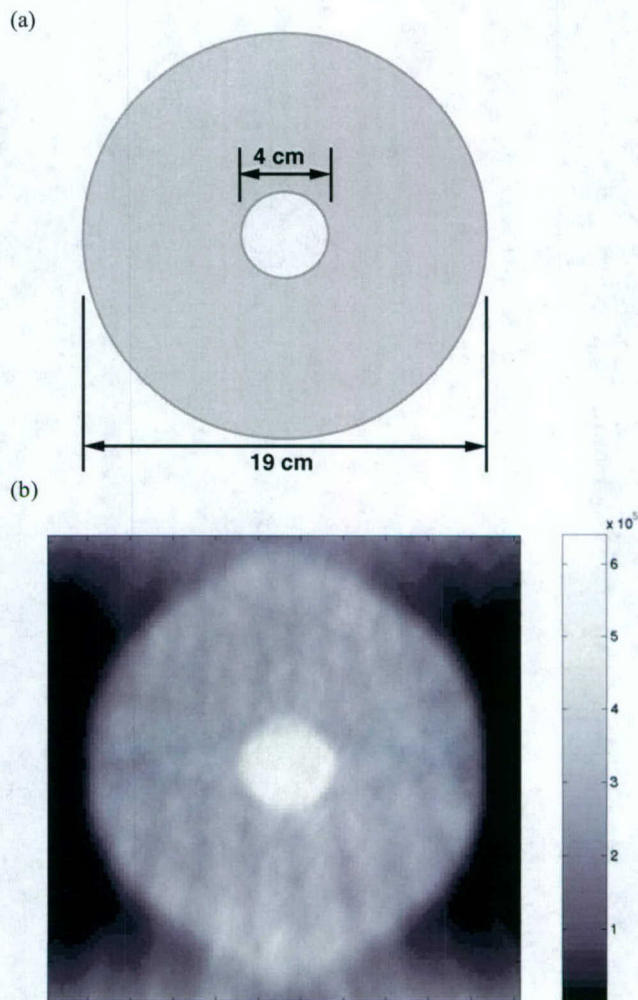


Fig. 7: (a) A concentric-cylinder phantom with three times higher activity density in the central cylinder than the outer cylinder. (b) Preliminary reconstructed image of the phantom using an iterative penalized ML algorithm. Initial total  $^{18}\text{F}$  activity density was 0.4  $\mu\text{Ci/ml}$  and the imaging time was 4 minutes. Image represents 78 Mcounts.

# Septa Design for a Prostate Specific PET Camera

Jinyi Qi, *Senior Member, IEEE*, Jennifer S Huber, *Member, IEEE*, Ronald H Huesman, *Fellow, IEEE*, William W Moses, *Senior Member, IEEE*, Stephen E Derenzo, *Fellow, IEEE*, Thomas F Budinger *Member, IEEE*,

**Abstract**—The recent development of new prostate tracers has motivated us to build a low cost PET camera optimized to image the prostate. Coincidence imaging of positron emitters is achieved using a pair of curved detector banks. The bottom bank is fixed below the patient bed, and the top bank, which is above the patient, moves upward for patient access and downward for maximum sensitivity. In this paper, we study the design of septa for the prostate camera using Monte Carlo simulations. The system performance is measured by the detectability of a prostate tumor and the conventional noise equivalent count (NEC). We have studied 27 septa configurations. The results show that septa design has a large impact on the lesion detection at a given activity concentration. At the background activity level of  $0.1 \mu\text{Ci/cc}$ , sparse septa with 8-crystal spacing outperforms the traditional two-dimension (inter-plane septa) and three-dimension (septaless) designs in terms of both the lesion detection and NEC. Significant differences are observed between the lesion detectability and NEC performance, indicating that the NEC may not be suitable for this lesion detection task.

## I. INTRODUCTION

Prostate cancer has a prevalence and diagnostic rate similar to breast cancer, with 360,000 new cases diagnosed each year and two million men affected by the disease in the United States. Prostate cancer suspicion is typically based on an elevated prostate-specific antigen (PSA) level or a suspicious node found during a digital rectal exam. Serum PSA values do not always correlate well with clinical diagnosis or outcomes. Palpation is subjective, insensitive and inexact. A new imaging technology for sensitive detection of early stage prostate cancer is needed to confirm initial diagnosis and help guide treatment decisions.

The recent development of new prostate tracers has shown promising results in detecting prostate cancer using carbon-11-choline [1]. This has motivated us to build a low cost PET camera optimized to image the prostate [2]. Coincidence imaging of positron emitters is achieved using a pair of curved detector banks. Fig. 1 shows the transaxial view of the camera. The bottom bank is fixed below the patient bed, and the top bank moves upward for patient access and downward for maximum sensitivity. Each bank consists of two axial rows of 20 block detectors ( $8 \times 8$  arrays of  $4.5 \times 4.5 \times 30 \text{ mm}^3$  BGO crystals), forming two arcs with a minor axis of 45 cm and major axis of 70 cm.

Individual detector modules are angled to point towards the camera center near the prostate location in order to reduce crystal penetration effects for annihilation photons originating in the prostate. This maintains high resolution selectively in the re-

gion of the prostate and is a unique feature of this non-circular camera geometry. Annihilation photons from other parts of the field of view (FOV) will suffer increased penetration effects, but these regions are less important.

Despite this special geometry, we are able to reconstruct nearly artifact free images around the prostate region by using an iterative reconstruction algorithm [2]. Since the average distance to the detectors is approximately one-half that of a conventional 2D PET system, the solid angle for a central source is approximately double for average-sized men. Thus, we expect to achieve improved detection efficiency at a lower cost.

In this paper we study septa designs to improve the detection of prostate cancer. Septa can reduce background events such as random coincidences and Compton scattered photons in the patient, but at an expense of reducing true coincidence events. Careful study is required to achieve the optimum balance. Previous research on the conventional PET scanners and the coincidence gamma cameras can be found in [3], [4], [5], [6], [7], [8], [9], [10], [11]. The uniqueness of this work is the specific application and special geometry of the prostate camera. To better assess the image quality, we measure the detectability of a prostate lesion using a prewhitening observer, in addition to the noise equivalent count (NEC) that was primarily used in previous studies. The results also demonstrate the limitation of NEC for lesion detection tasks.

## II. FIGURES OF MERIT

A popular figure of merit used to evaluate PET scanner design is the noise equivalent count, which is defined as

$$\text{NEC} = \frac{T^2}{T + S + kR} \quad (1)$$

where  $T$ ,  $S$ , and  $R$  are total number of true coincidences, scattered events, and random events, respectively. Here we use

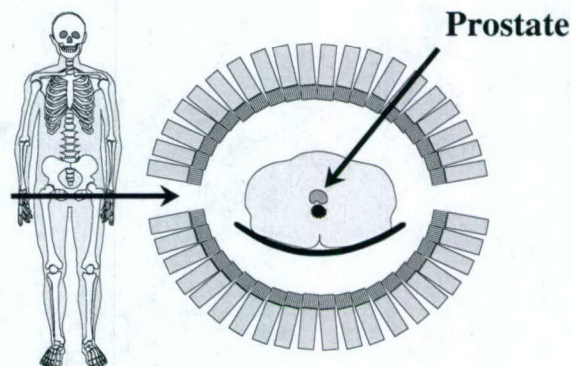


Fig. 1. A positron tomograph for prostate imaging [1].

This work is supported in part by Department of Defense grant number DAMD17-02-1-0081, by the Director, Office of Science, Office of Biological and Environmental Research, Medical Science Division of the U.S. Department of Energy under Contract No. DE-AC03-76SF00098, and by National Institutes of Health grant number R01 EB00194.

The authors are with the Department of Nuclear Medicine and Functional Imaging, Lawrence Berkeley National Laboratory, Berkeley, CA 94720, USA.

$k = 1$  assuming that the randoms are not pre-subtracted and the expectation of the randoms is estimated separately from the events in a delayed window.

Since our camera is designed specifically for imaging prostate tumors, we believe that it is more appropriate to measure system performance for this particular detection task. We choose a “signal-known-exactly, background-known-exactly” (SKE-BKE) task because the location of the prostate is relatively fixed and the background uptake is fairly uniform [1]. We use a prewhitening (PW) numerical observer, which is the ideal observer under Gaussian noise, to evaluate the lesion detectability. The performance of the PW observer measures the information content in the data for lesion detection.

Let  $\mathbf{h}_1$  and  $\mathbf{h}_0$  denote the expectations of the measurements with and without a lesion, respectively. The PW observer computes the following test statistic  $\eta$  for a given data set  $\mathbf{y}$

$$\eta(\mathbf{y}) = [\mathbf{h}_1 - \mathbf{h}_0]' \Sigma^{-1} \mathbf{y}, \quad (2)$$

where  $\Sigma$  is the ensemble covariance matrix of  $\mathbf{y}$ . A decision whether there is a lesion or not is then made by comparing this statistic to a pre-selected threshold. The detectability of the lesion can be measured by the signal-to-noise ratio (SNR) of  $\eta(\mathbf{y})$ , which is defined as

$$\text{SNR}^2 = \frac{[\eta(\mathbf{h}_1) - \eta(\mathbf{h}_0)]^2}{[\mathbf{h}_1 - \mathbf{h}_0]' \Sigma^{-1} [\mathbf{h}_1 - \mathbf{h}_0]}. \quad (3)$$

We model PET data as independent Poisson random variables with the expectation  $\bar{\mathbf{y}}$  related to the tracer distribution  $\mathbf{x}$  through an affine transform

$$\bar{\mathbf{y}} = \mathbf{P}\mathbf{x} + \mathbf{s} + \mathbf{r},$$

where  $\mathbf{P}$  is the projection probability matrix with the  $(i, j)$ th element denoting the probability of detecting an event from the  $j$ th voxel by the  $i$ th LOR,  $\mathbf{s}$  and  $\mathbf{r}$  denote the expectation of the scattered and random events, respectively.

Using this model, we have

$$\mathbf{h}_0 = \mathbf{P}\mathbf{b} + \mathbf{s} + \mathbf{r}, \quad (4)$$

$$\mathbf{h}_1 = \mathbf{P}\mathbf{b} + \mathbf{s} + \mathbf{r} + \mathbf{P}\mathbf{f}, \quad (5)$$

where  $\mathbf{b}$  is the normal uptake in a patient body and  $\mathbf{f}$  is the excessive uptake in a prostate lesion. Because the prostate lesion is small compare to the body, we ignore its effect on the scattered and random events and the Poisson noise. The covariance of the data in both situations can be approximated by

$$\Sigma^{-1} = \text{diag}[\mathbf{P}\mathbf{b} + \mathbf{s} + \mathbf{r}]. \quad (6)$$

Substituting (4)-(6) into (3) results

$$\text{SNR}^2 = \sum_i \frac{[\mathbf{P}\mathbf{f}]_i^2}{[\mathbf{P}\mathbf{b} + \mathbf{s} + \mathbf{r}]_i}. \quad (7)$$

We have shown in [12] that the SNR computed in (7) is the same as the SNR of a PW observer applied to images reconstructed using the maximum *a posteriori* (MAP) principle, but not using the filtered backprojection method. When  $\eta(\mathbf{y})$  is normally

distributed, the SNR is related to the area under the ROC curve by the error function [13]. Therefore, we use (7) to measure the lesion detectability.

Comparing (7) with (1), we see three differences: (1) NEC involves all LORs and is not specific to any local region, while SNR focuses on the LORs that pass through the lesion; (2) NEC computes the ratio of the sums, and SNR computes the sum of the ratios; (3) NEC treats all true coincidences as signal, and SNR treats only events from the lesion as signal. As a result, an increase in NEC does not suggest an increase or decrease in SNR without any other information, and vice versa.

### III. MONTE CARLO SIMULATION

We use Monte Carlo simulation to estimate the true coincidence rate, scatters and randoms under each septa configuration. The Monte Carlo simulation is conducted using the SimSET software<sup>1</sup>. Both Compton and photo-electric interactions are simulated in the patient body and septa. The patient body is modeled as an elliptical region with major and minor axes being 40 cm and 32 cm, respectively, which is the medium size of six randomly selected male persons in our department. It has uniform activity and the attenuation coefficient of water. The uniform uptake of C-11 choline was demonstrated by Hara *et al.* [1]. They also found that bladder accumulation is insignificant with correct time course (Fig. 2). The axial length of the body in the simulation is 60 cm, beyond which the activity has little contribution to the data.



Fig. 2. C-11 choline image of prostate cancer indicating a high (white) uptake in the prostate cancer and a low (gray) uniform uptake in the background. Images are provided by Hara *et al.*

The current version of SimSET is limited to circular ring PET scanners. To study the special geometry of the prostate camera, we model the septa as part of the attenuation object as shown in Fig. 3. The material of the septa is tungsten. The shape of the septa is modeled as the difference of two elliptical regions with major and minor axes of the inner one being 57 cm and 32 cm, respectively, and those of the outer one  $(1 + \alpha)57$  cm and  $(1 + \alpha)32$  cm, respectively, where  $\alpha$  is a variable that determines the radial length of septa. It ranges from 0.04 to 0.64. The thickness of the septa varies from 0.4 mm to 2.4 mm. The axial spacing between the septa varies from half a crystal (2.4 mm) to 16 crystals (77.6 mm). Table I summarizes the septa designs that we simulated.

The part of the body that is outside of the scanner FOV is surrounded by perfect absorber so that the acceptance of a photon

<sup>1</sup> Available at [http://depts.washington.edu/simset/html/simset\\_main.html](http://depts.washington.edu/simset/html/simset_main.html)

TABLE I  
PARAMETERS OF THE SIMULATED SEPTA DESIGNS

No.	Spacing (crystal)	thickness (mm)	$\alpha$
1	16		0.32
2	(no septa)		0.64
3	8	1.6	0.64
4		2.4	0.16
5		2.4	0.32
6		2.4	0.64
7	4	0.8	0.32
8		1.2	0.16
9		1.2	0.32
10		1.6	0.32
11	2	0.8	0.16
12		1.2	0.16
13		1.6	0.16
14	1	0.4	0.16
15		0.4	0.32
16		0.8	0.08
17		0.8	0.16
18		0.8	0.32
19		1.2	0.08
20		1.2	0.16
21		1.6	0.08
22		1.6	0.16
23		2.4	0.04
24	0.5	0.4	0.08
25		0.4	0.16
26		0.6	0.08
27		0.8	0.08

is completely determined by the septa. We use an extra long ring detector (axial length = 2000 cm) surrounding the whole object to catch all escaped photons. The hit position and direction of each photons on the ring detector are stored in a list-mode data file. Using these information, we are able to trace each photon back to the outer surface of the septa opening and then map the detection to a detector of the prostate camera. The detector is modeled as "black" material, but with a less-than-perfect detection efficiency (see Section V). We do not simulate any detector response (such as crystal penetration and inter-crystal scatter). Because septa affect image quality by blocking true, random, and scattered events, we believe that these detector responses have little effect on the *relative* performance of septa.

True coincidence events and scattered events are histogrammed separately. For all the results presented in this paper we use an energy threshold of 355 keV, except where noted otherwise. The singles rates are estimated by running the simulation in SPECT mode with the same number of photons. Random events are estimated from the singles rates by

$$r_k = \tau \cdot \text{singles}(i) \cdot \text{singles}(j), \quad (8)$$

where  $\text{singles}(i)$  and  $\text{singles}(j)$  are the singles rates of the two detectors forming the  $k$ th LOR, and  $\tau = 12\text{ns}$  is the coincidence timing window. All events are then corrected for deadtime as

described in Section IV.

To reduce the computational time, we first run short Monte Carlo simulations and rebin the data into one transaxial sinogram when calculating SNR using (7). From this initial results, we pick five designs and perform Monte Carlo simulations with high-statistics. The data are rebinned into 31 transaxial sinograms using single-slice rebinning for calculating SNR. To study the effect of noise in Monte Carlo simulations on the estimate of SNR, we generate a very high-count data set and treat it as noise-free. We then artificially add to it the same amount of Poisson noise as that in the simulation studies. The difference between the SNR calculated from the noisy data set and that calculated from the noise-free data set was found to be within 2%.

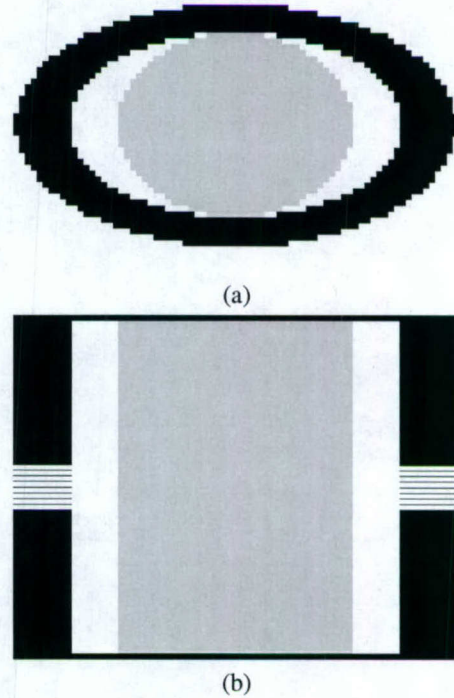


Fig. 3. Transaxial (a) and coronal (b) views through the center of the attenuation image used in the Monte Carlo simulation. The inner elliptical region is the patient body. The black band is the septa. The top and bottom axial planes contain perfect absorber to prevent photons from escaping from the axial openings. The parameters of septa shown in this figure are 2-crystal spacing, 1.2-mm thick, and  $\alpha = 0.16$ .

#### IV. DEADTIME MODEL

The deadtime of the camera is modeled similar to that described in [14]. Two parts of the deadtime are considered, one from the processing of single events in each detector block and the other from the coincidence processing circuit.

For each detector, the live time can be modeled as

$$d_i = e^{-\tau_{block} N \cdot \overline{\text{singles}}(i)} \quad (9)$$

where  $N$  is the number of detectors per detector block,  $\overline{\text{singles}}(i)$  is the average singles rate of the individual detectors within the block, and  $\tau_{block}$  is the time constant of the detector

block. The sensitivity of the  $k$ th LOR due to the detector block deadtime is then

$$n_k = d_i * d_j, \quad (10)$$

where  $i$  and  $j$  are the indices of the two detectors forming the  $k$ th LOR.

The system wide coincidence processing live time is

$$\text{Coinc. Live} = e^{-\tau_{sys} \text{Coinc. Load}} \quad (11)$$

where  $\tau_{sys}$  is the time constant, and *Coinc.Load* is the ideal count rate experienced by the coincidence processing circuit. It is calculated as

$$\text{Coinc. Load} = \sum_k (t_k + s_k + 2r_k) n_k, \quad (12)$$

where  $t_k$ ,  $s_k$ , and  $r_k$  are the ideal count rates of the trues, scatters, and randoms in the  $k$ th LOR, respectively. The factor of 2 accounts for the randoms in both prompt and delayed windows<sup>2</sup>. The overall sensitivity of the  $k$ th LOR due to the deadtime loss is  $n_k * \text{Coinc. Live}$ .

## V. NORMALIZATION

A 20 cm diameter, 19 cm long uniform cylinder with activity concentration of  $0.06 \mu\text{Ci/cc}$  was scanned in an ECAT HR scanner (CTI PET systems, Knoxville, TN) in 3D mode. The measured singles rates are compared with that obtained from the Monte Carlo simulation of the same cylinder scan to calculate the detector efficiency. After scaling the simulation result with this calculated detector efficiency ( $=0.49$ ), the true coincidence, scatters, and randoms are compared. Fig. 4 shows the measured and simulated projection profiles. The simulated scatter profile matches very well with the real measurement. The slight discrepancy between the measured and simulated true coincidence from  $-100$  mm radial offset to the radial center is due to the attenuation of the patient bed, which is not modeled in the simulation. The comparison between the randoms calculated from singles rates and that measured using delayed window shows a nearly perfect match (a ratio of 1.0). The simulated event rate of trues plus scatters also matches the measured event rate well (a ratio of 0.97).

To estimate the time constants  $\tau_{block}$  and  $\tau_{sys}$  in the dead-time model, another uniform cylinder (the same geometry) with activity concentration of  $0.6 \mu\text{Ci/cc}$  was scanned in the ECAT HR scanner. The system deadtime as reported by the scanner is about 23%. The fitted time constants are  $\tau_{block} = 2.2 \mu\text{s}$  and  $\tau_{sys} = 118 \text{ ns}$ .

## VI. RESULTS

### A. Initial results

We ran an initial study on all 27 different septa configurations (Table I) with short Monte Carlo simulations and rebinned the data into one transaxial sinogram to reduce noise. Fig. 5 shows the SNR and NEC of all the septa designs at different background activity levels. The simulated lesion is a 2.5-cm diameter sphere located at the center of the FOV. The lesion to

<sup>2</sup>Here we assume that the events in the delayed window will be used to estimate the expectation of the random events.

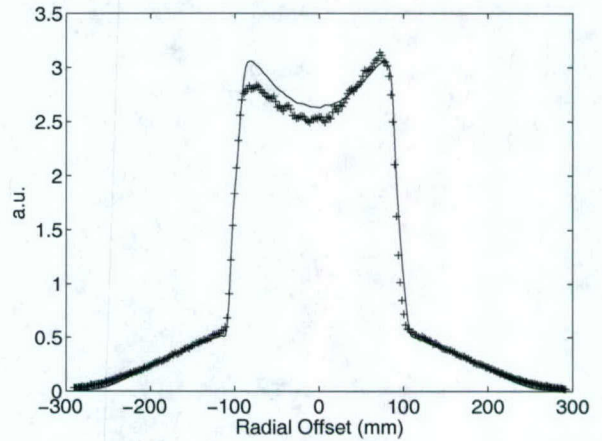


Fig. 4. Comparison between the measured ('+') and the simulated (solid line) projection profiles.

background activity ratio is 2:1. The scan duration is 1 minute. Both lesion detectability and NEC show that longer and thicker septa are preferred for high activity concentration due to the increase in random fraction and deadtime. However, doubling the length often has a stronger effect than doubling the thickness. The lesion detectability curves clearly show that sparse septa (more spacing) can improve lesion detection with the best peak SNR achieved by design no. 6 around  $1.0 \mu\text{Ci/cc}$  background activity level.

For the application of the prostate camera, we expect that the typical background activity concentration will be around  $0.1 \mu\text{Ci/cc}$ , which corresponds to a uniform uptake of 7.5-mCi injection into a 75-kg patient. In Fig. 6, we plot the SNR and NEC at  $0.1 \mu\text{Ci/cc}$  for all the septa designs. The results show that design no. 5 outperforms others in terms of both lesion detection and NEC.

### B. High-Statistics Simulation Results

From the initial results we picked five designs for a more careful study. We ran Monte Carlo simulation with high statistics. Instead of rebinning the data into one sinogram, we rebin data into 31 plane using single slice rebinning. Fig. 7 shows the new SNR results. Comparing to Fig. 5, we found that the absolute SNR value increased and the intersection points between curves shifted. At  $0.1 \mu\text{Ci/cc}$ , the best design is still no. 5, but the performance is close to design no. 6..

### C. Prostate Positioning

In all above studies the prostate is placed at the axial center of the FOV. However, the exact positioning is difficult in practice even with ultrasound guidance. Here we study the change in detectability of a prostate lesion when the prostate is positioned away from the axial center. Fig. 8 shows the SNR of detecting a prostate tumor with different axial displacement from the center of FOV. The results show that septa with larger spacing are more sensitive to the position of the prostate. When the prostate is placed 2-cm off-center axially, the performance of design no. 5 drops below that of design no. 10. Note that NEC does not change with tumor location because it is a global mea-

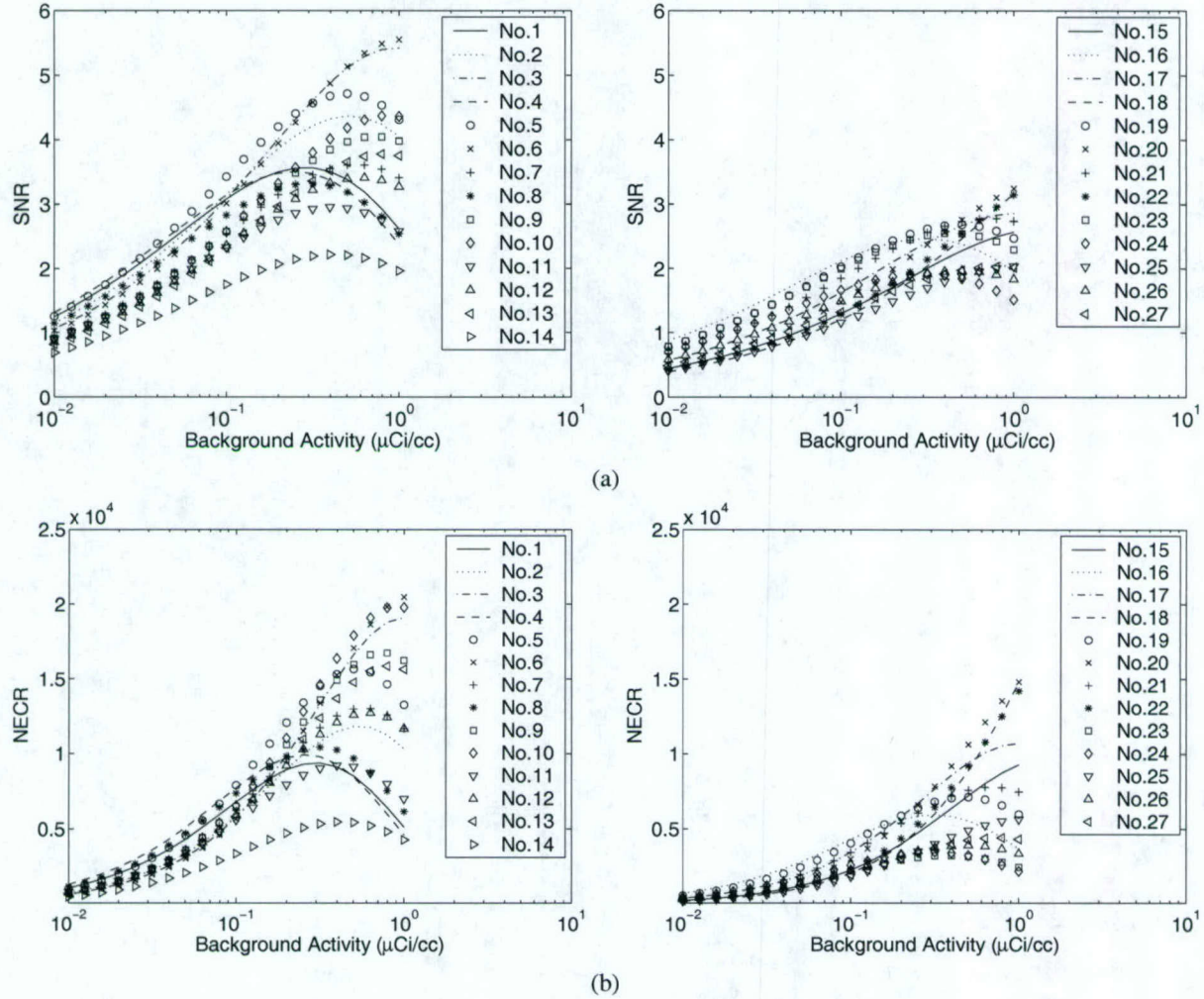


Fig. 5. Performance of 27 septa designs as a function of background activity levels. (a) lesion detectability plots; (b) NEC plots. The legend refers to the design number shown in Table I.

sure.

Fig. 9 shows the mean SNR when the prostate positioning error is modeled as a Gaussian random variable with a standard deviation of 1 cm. Under this model design no. 5 achieves the highest average SNR when background activity is at  $0.1 \mu\text{Ci/cc}$ .

#### D. Energy resolution

We studied the effect of energy resolution on septa design by varying the energy threshold in the Monte Carlo simulation. Fig. 10 shows the performance of a system with perfect energy resolution (energy threshold = 511 keV). Comparing Fig. 10 and Fig. 7, we found that good energy resolution increases the lesion detectability and favors less septa due to the better rejection of events scattered inside the patient body and the septa.

### VII. DISCUSSION

**SNR vs. NEC:** In Section II, we compared the theoretical difference between SNR and NEC and pointed out that without additional information, an increase in NEC does not suggest an increase or decrease in SNR. However, the experimental results in Figs. 5 and 6 show that some correlation may exist between SNR

and NEC. The reason behind this is that we fixed the background and lesion in the study. With such constraints, NEC tends to correlate with SNR, but the extent of the correlation depends on the background and lesion properties. If the parameters under study include background and lesion variability, the correlation will reduce. For example, as we change the prostate location, SNR changes significantly, but NEC remains the same. The fact that both SNR and NEC favor design no. 5 at  $0.1 \mu\text{Ci/cc}$  for the center lesion is purely coincidental because SNR and NEC do not agree with each other at all activity levels and all lesion locations. It is difficult to predict the exact correlation between NEC and SNR for each experiment, and more often than not, a system that gives the highest NEC is not the best for lesion detection. Thus, it is desirable to use a task-specific figure of merit, such as SNR, to evaluate system performance for lesion detection.

### VIII. CONCLUSION

We have conducted Monte Carlo simulations to study the effect of septa configuration on lesion detection. The results clearly show that properly designed sparse septa can improve lesion detection over the traditional two-dimension (inter-plane

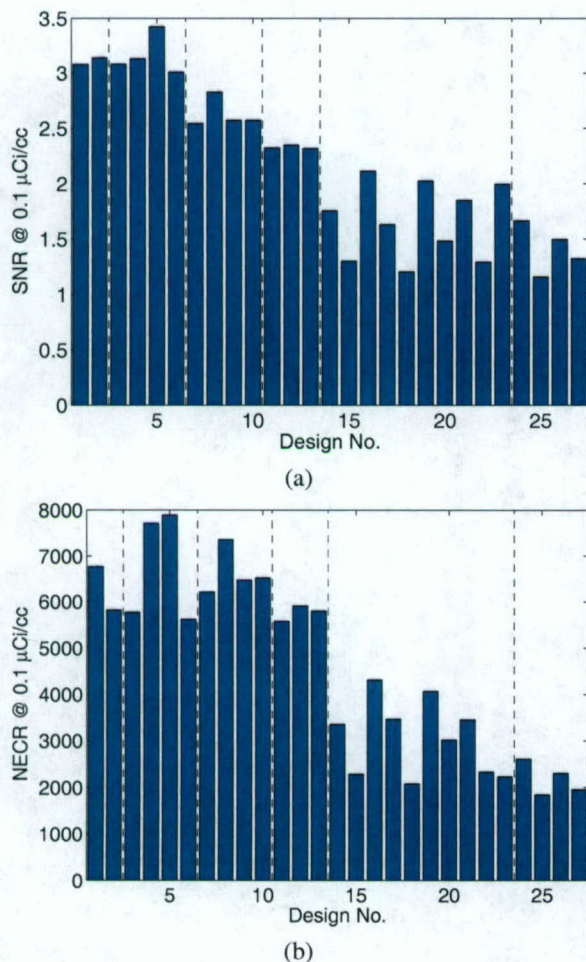


Fig. 6. Performance of all the septa designs at  $0.1 \mu\text{Ci/cc}$ . (a) lesion detectability; (b) NEC. The design number refers to Table I. The dashed lines indicate the change in septa spacing.

septa) or three-dimension (septaless) configurations. Among all the designs that we studied here, we found that the septa with 8-crystal spacing give the best lesion detection and NEC at the background activity level of  $0.1 \mu\text{Ci/cc}$ . In future work we will construct the septa and evaluate their performance using real measurements.

#### IX. ACKNOWLEDGMENTS

The authors would like to thank Robert Harrison at the University of Washington Medical Center, and Eric Frey and Ben Tsui at the Johns Hopkins University for their help in the SimSET software, and to thank Harrison Barrett at the University of Arizona and the anonymous reviewers for their insightful comments.

This work is supported in part by Department of Defense grant number DAMD17-02-1-0081, by the Director, Office of Science, Office of Biological and Environmental Research, Medical Science Division of the U.S. Department of Energy under Contract No. DE-AC03-76SF00098, and by National Institutes of Health grant number R01 EB00194.

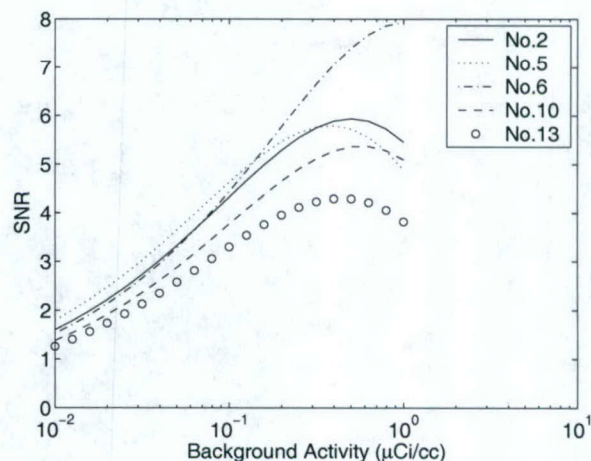
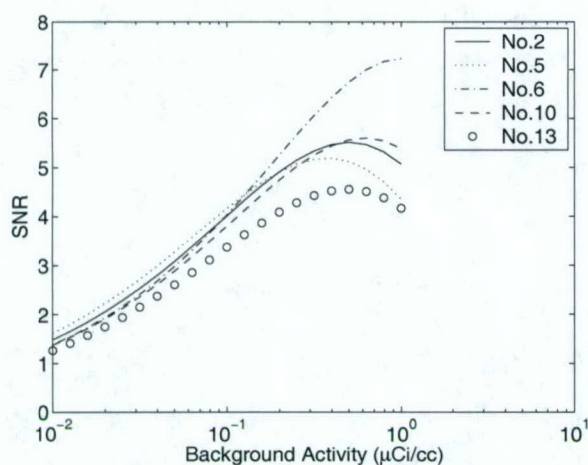


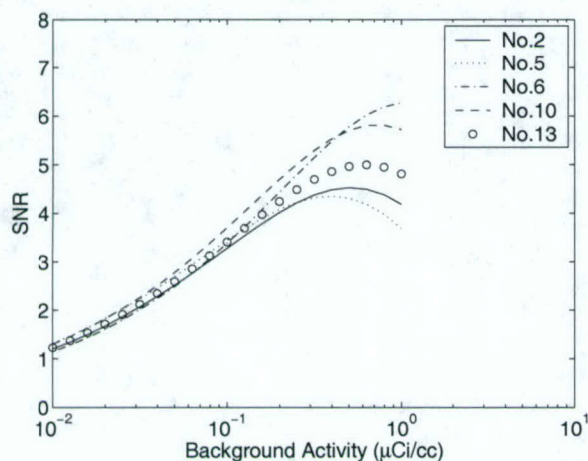
Fig. 7. Performance of five septa designs when data are rebinned into 31 sino-gram planes. The design number refers to Table I.

#### REFERENCES

- [1] T. Hara, N. Kosaka, and H. Kishi, "PET imaging of prostate cancer using carbon-11-choline," *J. Nucl. Med.*, vol. 39, pp. 990–995, 1998.
- [2] J. Huber, S. Derenzo, J. Qi, W. Moses, R. Huesman, and T. Budinger, "Conceptual design of a compact positron tomograph for prostate imaging," *IEEE Trans. Nucl. Sci.*, vol. 48, pp. 1506–1511, 2001.
- [3] C. Thompson, "The effect of collimation on scatter fraction in multi-slice PET," *IEEE Trans. Nucl. Sci.*, vol. 35, pp. 598–602, 1988.
- [4] L. E. Adam, J. S. Karp, and G. Brix, "Investigation of scattered radiation in 3D whole-body positron emission using Monte Carlo simulations," *Phys. Med. Bio.*, vol. 44, pp. 2879–2895, 1999.
- [5] R. Lecomte, "Analytical study of performance in a 3D PET scanner," *Phys. Med. Bio.*, vol. 37, pp. 623–634, 1992.
- [6] M. Aykac, J. Uribe, H. Baghaei, H. Li, Y. Wang, Y. Liu, T. Xing, and W.-H. Wong, "Septa design study for volumetric imaging in positron emission tomography," *IEEE Trans. Nucl. Sci.*, vol. 49, pp. 2097–2102, 2002.
- [7] T. Hasegawa, E. Tanaka, T. Yamashita, M. Watanabe, T. Yamaya, and H. Murayama, "A Monte Carlo simulation study on coarse septa for scatter correction in 3-D PET," *IEEE Trans. Nucl. Sci.*, vol. 49, pp. 2133–8, 2002.
- [8] H. Baghaei, W. H. Wong, J. Uribe, H. Li, M. Aykac, Y. Wang, Y. Liu, T. Xing, and R. Farrell, "Brain lesion detectability studies with high resolution PET operating in no-septa and partial septa configurations," *IEEE Trans. Nucl. Sci.*, vol. 50, pp. 1364–1369, 2003.
- [9] C. J. Groiselle, Y. D'Asseler, J. A. Kolthammer, C. G. Matthews, and S. J. Glick, "A Monte Carlo simulation study to evaluate septal spacing using triple-head hybrid PET imaging," *IEEE Trans. Nucl. Sci.*, vol. 50, pp. 1339–46, 2003.
- [10] T. C. Rust and D. J. Kadrmas, "Survey of parallel slat collimator designs for hybrid PET imaging," *Phys. Med. Bio.*, vol. 48, pp. N97–104, 2003.
- [11] S. J. Glick, C. J. Groiselle, J. Kolthammer, and R. Z. Stodilka, "Optimization of septal spacing in hybrid PET using estimation task performance," *IEEE Trans. Nucl. Sci.*, vol. 49, pp. 2127–32, 2002.
- [12] J. Qi and R. H. Huesman, "Theoretical study of lesion detectability of MAP reconstruction using computer observers," *IEEE Trans. Med. Im.*, vol. 20, pp. 815–822, 2001.
- [13] H. H. Barrett, G. K. Abbey, and E. Clarkson, "Objective assessment of image quality. III. ROC metrics, ideal observers, and likelihood-generating functions," *Journal of Optical Society of America A*, vol. 15, pp. 1520–1525, 1998.
- [14] L. Eriksson, K. Wienhard, and M. Dahlbom, "A simple data loss model for positron camera systems," *IEEE Trans. Nucl. Sci.*, vol. 41, pp. 1566–1570, 1994.



(a)



(b)

Fig. 8. Detectability of a prostate tumor with different axial displacement: (a) 1 cm and (b) 2 cm.

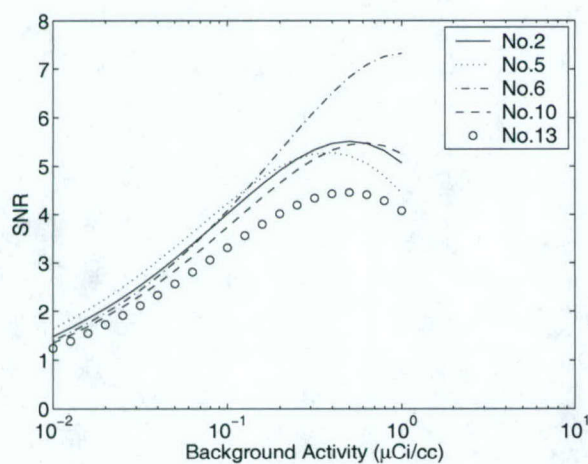
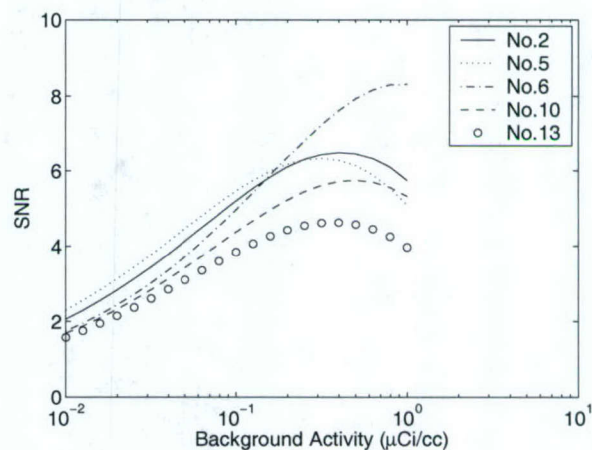
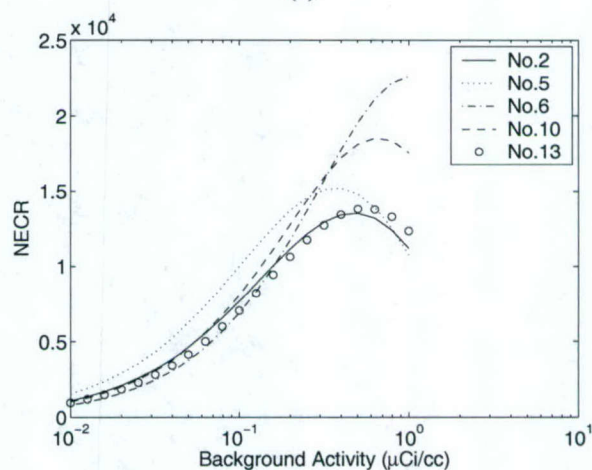


Fig. 9. The mean SNR when the prostate positioning error is a Gaussian random variable with a standard deviation of 1 cm.



(a)



(b)

Fig. 10. Performance of a system with perfect energy resolution (energy threshold = 511 keV). (a) lesion detectability; (b) NEC. The design number refers to Table I.

# The Development of a Compact Positron Tomograph for Prostate Imaging

J. S. Huber, *Member, IEEE*, J. Qi, *Member, IEEE*, S. E. Derenzo, *Fellow, IEEE*, W. W. Moses, *Senior Member, IEEE*, R. H. Huesman, *Fellow, IEEE*, and T. F. Budinger, *Member, IEEE*

**Abstract**—We give design details and expected image results of a compact positron tomograph designed for prostate imaging that centers a patient between a pair of external curved detector banks (ellipse: 45 cm minor, 70 cm major axis). The bottom bank is fixed below the patient bed, and the top bank moves upward for patient access and downward for maximum sensitivity. Each bank is composed of two rows (axially) of 20 CTI PET Systems HR+ block detectors, forming two arcs that can be tilted to minimize attenuation. Compared to a conventional PET system, our camera uses about one-quarter the number of detectors and has almost two times higher solid angle coverage for a central point source, because the detectors are close to the patient. The detectors are read out by modified CTI HRRT data acquisition electronics. The individual detectors are angled in the plane to point towards the prostate to minimize resolution degradation in that region. Inter-plane septa extend 5 cm beyond the scintillator crystals to reduce random and scatter backgrounds. Average- to large-size patients will not be fully encircled by detector rings, causing incomplete sampling due to the side gaps. Monte Carlo simulations (including 20% randoms and 30% scatter fractions) demonstrate the feasibility of detecting and differentiating prostate tumors with a tumor to background ratio of 2:1, using a number of counts that should be achievable with a 6 minute scan after a 10 mCi injection (e.g., carbon-11 choline). Simulations also predict minimal blurring in the 10 cm diameter central region for a wide range of patient sizes.

## I. INTRODUCTION

WE present the development of a compact positron tomograph optimized to image the prostate. This instrument images radiopharmaceuticals that specifically localize in the prostate to confirm the presence, absence or progression of disease. It has approximately four times fewer detectors than a conventional whole-body positron emission tomograph (PET), which will reduce the cost and increase clinical availability.

Prostate cancer has a prevalence and diagnostic rate similar to breast cancer, with 360,000 new cases diagnosed each year and two million men affected by the disease in the United States. Prostate cancer suspicion is typically based on an elevated prostate-specific antigen (PSA) level or a suspicious

node found during a digital rectal exam. Serum PSA values do not always correlate well with clinical diagnosis or outcomes [1-3]. Palpation is subjective, insensitive and inexact; more than half of all cancers detected today are not palpable. Treatment decision is based mainly on biopsy confirmation of prostate cancer, but the diagnostic accuracy of prostate biopsies is problematic. Typical treatment options include radical prostatectomy, external beam irradiation, brachytherapy (interstitial implantation of radioactive seeds), androgen ablation (hormone) therapy, or "watchful waiting." A major problem with prostatic cancer therapy is the question of when to treat or whether to treat at all. This is particularly problematic in the case of an increased PSA level with non-diagnostic repeated biopsies or after a prostatectomy. A new imaging technology for sensitive detection of early stage prostate cancer is needed to confirm initial diagnosis and help guide treatment decisions. In addition, a new method is needed to assess response shortly after treatment intervention.

In order to help meet these needs, we are building a compact PET camera optimized to image the prostate. Functional PET imaging will help detect malignant tumors in the prostate and/or prostate bed to confirm an elevated PSA level, as well as possibly help determine tumor "aggressiveness" based on metabolic uptake levels, in order to help guide whether to treat suspected prostatic cancer. Although not optimized to detect distant metastatic disease, this compact PET camera should also image local spread beyond the prostate bed to help guide treatment decisions such as whether a narrow or wide irradiation treatment field is needed.

Promising PET radiopharmaceuticals have recently demonstrated outstanding results in the sensitive detection of prostate cancer, inspiring a new interest in using PET for prostate cancer imaging. Consistent with the evidence of increased pool size of choline in prostate cancer [4, 5], Hara and co-workers demonstrated prostate tumor uptake by [ $^{11}\text{C}$ ]choline. They find that: [ $^{11}\text{C}$ ]choline clears the blood faster than FDG; its uptake in prostate tumors is significantly higher than in normal and surrounding tissues [6, 7], providing excellent tumor/normal contrast; and bladder accumulation is minimal if the correct time course is chosen [8] which is a major advantage over FDG. Additionally, they observe that [ $^{11}\text{C}$ ]choline PET is more sensitive for detecting bone metastases than bone scintigraphy. Therefore,

Manuscript received December 10, 2002. This work was supported in part by the Director, Office of Science, Office of Biological and Environmental Research, Medical Science Division of the U.S. Department of Energy under Contract No. DE-AC03-76SF00098 and in part by Department of Defense grant number DAMD17-02-1-0081.

J. S. Huber, J. Qi, S. E. Derenzo, W. W. Moses, R. H. Huesman and T. F. Budinger are with the Lawrence Berkeley National Laboratory, Mailstop

55-121, 1 Cyclotron Road, Berkeley, CA 94720 USA (telephone: 510-486-6445, e-mail: [jshuber@lbl.gov](mailto:jshuber@lbl.gov)).

[ $^{11}\text{C}$ ]choline is an attractive PET tracer for imaging primary and metastatic tumors of the prostate and potentially for other regions of the body [9-13]. Fig. 1 shows a [ $^{11}\text{C}$ ]choline image of prostate cancer before and after therapy, demonstrating the ability to detect prostate carcinoma using choline and possibly its analogs. Other  $^{11}\text{C}$  radiopharmaceuticals are also under investigation for prostate cancer PET imaging, including [ $^{11}\text{C}$ ]acetate and [ $^{11}\text{C}$ ]methionine.

$^{18}\text{F}$  imaging has the advantage of a longer half-life, which increases clinical viability since an on-site cyclotron facility would not be necessary (as it would for  $^{11}\text{C}$  imaging). Many groups have shown that PET imaging with [ $^{18}\text{F}$ ]fluorodeoxyglucose (FDG) is not a good technique for prostate cancer diagnosis, because FDG is not very prostate specific (with a SUV of typically  $\sim 2$ ) and the uptake is overcome by background primarily due to bladder accumulation. The SUV (standard uptake value) is the ratio of activity in the target tissue to the average activity in the body. However, there are several other  $^{18}\text{F}$  radiopharmaceuticals currently under investigation for prostate cancer imaging, including [ $^{18}\text{F}$ ]fluorocholine (FCH) [14, 15]. PET images using [ $^{18}\text{F}$ ]fluorocholine demonstrate high standardized uptake values (*e.g.*, SUV of 8), indicating that FCH is well localized in the prostate cancer and can be imaged with good resolution if a short scan time ( $\sim$ five minutes) is used. Therefore, [ $^{18}\text{F}$ ]fluorocholine is also an attractive PET tracer for imaging primary and metastatic tumors of the prostate.

## II. CAMERA DESIGN

### A. Overview

These new prostate tracers have motivated us to build a low cost PET camera optimized to image the prostate. Coincidence imaging of positron emitters is achieved using a pair of external curved detector banks, one placed above and one below the patient. Fig. 2 shows the transaxial and sagittal views of the camera. The bottom bank is fixed below the patient bed, and the top bank moves upward for patient access and downward for maximum sensitivity. Each bank consists of two axial rows of 20 CTI ECAT HR+ block detectors, forming two arcs with a minor axis of 45 cm and major axis of 70 cm. Our prostate camera has about one-fourth the number of detectors as in a conventional PET system because: (a) the patient is not fully encircled in 2D, (b) an elliptical shape is used instead of a circular one, and (c) the axial coverage is only 8 cm. However, since the average distance to the detectors is approximately one-half that of a conventional 2D PET system, the solid angle for a central source is approximately double for average-sized men. Thus, we expect to achieve improved detection efficiency at a lower cost.

Individual detector modules are angled to point towards the camera center near the prostate location in order to reduce penetration effects (in the detector) for annihilation photons originating in the prostate. This increases resolution

selectively in the region of the prostate and is an unique feature for a non-circular camera geometry. Annihilation photons from other parts of the field of view (FOV) will suffer increased penetration effects, but these FOV regions are less important. Both detector banks can be tilted to image the prostate while minimizing attenuation (*i.e.*, above the buttocks and below the stomach, see Fig. 2), but the gantry allows zero tilt for thin patients. A patient of average size is not fully encircled in 2D, which results in irregular and incomplete sampling due to the side gaps. Despite this incomplete sampling, we are able to reconstruct nearly artifact free images in the region of interest by using an iterative reconstruction algorithm [16].

The camera design also includes shielding [16]. Inter-plane septa extend 5 cm beyond the scintillator crystals to reduce background events from random coincidences and from photons that Compton scatter in the patient. Lead shields are also used on the ends to reduce activity from outside the field of view.

### B. Electronics

Our camera uses modified commercial components in a novel geometry. We are using 80 CTI ECAT HR+ block detectors that are three attenuation lengths thick for good detection efficiency with narrow detector elements (*i.e.*,  $8 \times 8$  arrays of  $4.5 \times 4.5 \times 30 \text{ mm}^3$  BGO crystals) to achieve good spatial resolution. We are using modified front end, coincidence, and readout electronics developed by CTI for the HRRT brain imaging PET camera, as shown in Fig. 3. Since we are creating a non-standard camera with HR+ and HRRT components, a custom conversion board is necessary. Events are detected and assigned an arrival time, the crystal of interaction is identified, energy qualification is performed, and a digital word is formed using 28 CTI HRRT Analog Subsection boards. The output signals from the Analog Subsection boards are then multiplexed by six custom Detector Head Interface (DHI) boards, which are based on the CTI HRRT DHI design but each services a maximum of 15 (rather than 117) detector modules. We are using six DHI boards to allow coincidences between detector modules within the same bank and plane. A CTI Coincidence Processor identifies singles events in the different DHI boards that are in coincidence, and the output is sent to a Pentium-based computer system that accumulates the coincident data, reconstructs the images, and displays them.

We previously reported on the conceptual design of this prostate camera [16]. We have moved from the idea stage into the building stage. We have acquired all HR+ detector blocks and electronics boards. We are currently testing the CTI electronics and modifying the DAQ software for our system.

### C. Gantry

The gantry and electronic housing is designed and under construction. We still need to design and build the septa and patient bed. Fig. 4 shows a photograph of the top and bottom aluminum arc plates with some of the CTI ECAT HR+ detector modules mounted in place. The detector

modules are individually positioned to point towards the center of the camera, as discussed in Section IIA.

Fig. 5 shows a 3-D drawing of the camera with many of the gantry and electronic housing details. The upper bank is mounted onto a main aluminum back-plate in order to control the vertical motion using a hand-crank, allowing upward movement for patient access and downward to maximize sensitivity. A second hand-crank is used to adjust the overall tilt of both upper and lower banks. The rear end of Fig. 5 also shows the electronic housing. The six DHI boards are mounted horizontally to the housing that holds their corresponding Analog Subsection boards. The Coincidence Processor board is mounted onto the cabinet door for compactness. The  $\pm 5V$  and high voltage power supplies are mounted on the far end.

### III. EXPECTED PERFORMANCE

#### A. Point Source Grid

To determine the size of the region of high spatial resolution, we have performed statistical noise-free simulations. Fig. 6 shows reconstructed point sources in a grid. Data are generated with interactions throughout the crystal, assuming an attenuation length of 10 mm in the BGO crystal. A preliminary iterative maximum likelihood algorithm is used in the reconstruction without correcting for detector penetration. The point sources are 5 cm apart, and the grid covers the majority of the field of view. All point sources are clearly visible in the image (black = high uptake). As expected, increased radial blurring due to penetration effects is seen in the region representing the outer edge of the patient. Since we are optimizing resolution at the center near the prostate at the price of resolution at the edges, distant metastases will suffer from some resolution degradation. However, good resolution is observed in the 10 cm diameter central region near the prostate. In Fig. 6, the central point has both a radial and tangential fwhm of 2 mm. More representative of the expected spatial resolution, the surrounding eight points have a radial fwhm of 4 mm and tangential fwhm of 3 mm. Improved resolution for more distant points is expected when the reconstruction corrects for detector penetration, although this process increases the statistical noise in the reconstruction.

Assuming that the detector arcs are rigid with a fixed focal spot for each arc, both focal spots are at the center for the 'nominal' gap separation. The above simulation (Fig. 6) assumed this 'nominal' gap distance. In order to investigate the effect of varying the gap between the arcs, the simulation is repeated for a gap range of  $\pm 5$  cm when the focal spots are no longer in the center. The same minimal blurring within a 10 cm diameter central region is observed for both cases, indicating that a wide range in patient size will not compromise the resolution near the prostate. Fig. 7 shows the reconstructed point source grid with the gap distance increased by +5 cm from 'nominal' position.

The above results show that we can achieve similar resolution in the 10 cm diameter center region as an ECAT

HR+ scanner. Using the nominal configuration, we also compute the signal to noise ratio (SNR) of an ideal observer for detecting a small lesion at the grid locations. The background is modeled as an uniform elliptical region (major axis = 40 cm, minor = 30 cm). For the central point, the resulting SNR of the new system is about 27% higher than that of an ECAT HR+ scanner under the same situation, and the SNR is about 20% higher for the surrounding eight points. This indicates that while the resolution is similar, the increase in sensitivity can still improve lesion detection. The above computation is for one 2D direct plane. No random or scattered events are modeled for either scanner.

#### B. Extended Sources

Monte Carlo methods are used to study the reconstruction of extended sources. Reconstructions are performed with an iterative maximum likelihood technique that assumes statistical noise representing 745 kcounts/slice, a tumor activity concentration that is two times the background activity concentration, 30% scatter fraction, and 20% randoms fraction. The reconstructions are then post-filtered with a very conservative Gaussian function of  $\sigma = 1$  pixel = 2 mm. We simulate self-attenuation by assuming a constant attenuation coefficient of 0.0095/mm inside the body. Coincidences between detector modules within the same bank and plane are allowed. Fig. 8(a) shows the body outline of a patient with an extended "prostate" source (2.5 cm diameter circle) with "tumors" in the upper right and lower left quadrants. Fig. 8(b) shows a reconstructed image of the phantom with "tumors" in the upper right and lower left quadrants clearly visible (white = high uptake), demonstrating that we can reconstruct nearly artifact-free images as well as detect and differentiate partial and whole prostate tumors. Our preliminary rate calculations indicate that 745 kcounts per imaging plane will be achievable with a six minute scan after a 10 mCi injection [16]. A relatively short value of six minutes is chosen to demonstrate that good images can be obtained even if the bladder fills rapidly. All published [ $^{11}C$ ]choline or [ $^{18}F$ ]fluorocholine studies done to date have used three minutes or longer (up to 30 minutes) imaging times.

#### C. Data Correction

Our design has sufficient room to incorporate a single photon or positron emitting source for transmission scans, but it would add to the camera cost. We plan to correct without an additional source using calculated attenuation coefficients based on body contours and an uniform attenuation coefficient [16]. Anatomical boundaries can be obtained from the outer edges of emission sinograms acquired from transverse sections [17]. It may also be possible to use heterogeneous attenuation coefficients by identifying tissue types (e.g., soft tissue, bone, and air) based on x-ray CT images.

Because of the unusual geometry of our camera, the sensitivity of each line of response depends on the distance between the two detectors and the face angles of the two detectors; the shorter the distance is, the higher the

sensitivity. Normalization will include geometric correction (sensitivity changes caused by the septa that are not modeled in the solid angle computation), block effect correction, individual detector sensitivity correction, and dead time correction. These factors will be obtained using a scan of a uniform activity plane source such as used in conventional PET scanners. However, because of our specialized geometry and lack of rotational symmetry, the method for deriving the first two factors will be different from that of circular systems and may require a longer scan time to achieve good count statistics.

Random events will be estimated using the delayed window technique. Instead of pre-subtracting histogrammed data, delayed events will be saved in the list mode data stream with a tag to distinguish them from prompt events. For our statistical reconstruction algorithm, the estimated randoms will be included in the forward model in reconstruction.

#### IV. DISCUSSION

This project is in its initial building phase, so there are many remaining uncertainties, including which radiopharmaceutical will be used, the specific requirements for the radiopharmaceutical and imaging procedure, and the accuracy that physicians would require to perform effective diagnosis and evaluate response to therapy. However, new PET radiopharmaceuticals have recently demonstrated promising results in the sensitive detection of prostate cancer. This PET camera design is also likely to out-perform whole body PET for this task, as the higher sensitivity will help for the short scans that appear to be necessary with choline-like radiopharmaceuticals.

Accurate patient positioning is also critical due to the limited (8 cm) axial extent of the camera. A manually placed external or trans-rectal positron-emitting source could be used to position the prostate near the center of the FOV of the camera. Alternatively, the prostate is visible in ultrasound images acquired with an external transducer, and these images could be used to position the patient bed.

Finally, as Fig. 1 shows, it is difficult to identify features other than the prostate (and possibly the bladder) in the PET images. Local anatomic information is highly desirable to determine the location of the disease within the prostate, as well as to determine whether the disease has spread to the prostate bed. This information could be obtained with dual modality imaging. X-ray CT provides excellent images of the abdomen, but the cost is relatively high. Ultrasound imaging with a trans-rectal probe provides reasonable detail in the region of the prostate and the cost of an ultrasound unit is significantly less than that of a CT imager, so we plan to explore adding co-registered ultrasound imaging capability.

#### V. CONCLUSION

Promising new PET tracers for prostate cancer, such as [ $^{11}\text{C}$ ]choline and [ $^{18}\text{F}$ ]fluorocholine, have motivated us to design and build a low cost PET camera optimized for prostate imaging. Monte Carlo simulations demonstrate the

feasibility of detecting and differentiating partial and whole prostate tumors with a tumor to background ratio of 2:1, using a six minute scan after a 10 mCi injection. Simulations also predict minimal blurring in the 10 cm diameter central region for a wide range in patient size. Thus, we are currently building a camera that will image prostate tumors with good spatial resolution and image contrast at low cost relative to commercial PET scanners.

#### VI. ACKNOWLEDGMENT

We thank Dr. Hara from the International Medical Center of Japan for providing the PET images presented in Fig. 1 of this paper. We also thank Dr. Nutt from CPS Innovations for providing detectors and electronics. This work was supported in part by the Director, Office of Science, Office of Biological and Environmental Research, Medical Science Division of the U.S. Department of Energy under Contract No. DE-AC03-76SF00098 and in part by Department of Defense grant number DAMD17-02-1-0081. Reference to a company or product name does not imply approval or recommendation by the University of California or the U.S. Department of Energy to the exclusion of others that may be suitable.

#### VII. REFERENCES

1. H. I. Scher and L. W. Chung, "Bone metastases: improving the therapeutic index," *Semin Oncol*, vol. 21, pp. 630-56, 1994.
2. H. I. Scher, M. Mazumdar, and W. K. Kelly, "Clinical trials in relapsed prostate cancer: defining the target," *J Natl Cancer Inst*, vol. 88, pp. 1623-34, 1996.
3. M. A. Eisenberger and W. G. Nelson, "How much can we rely on the level of prostate-specific antigen as an end point for evaluation of clinical trials? A word of caution! [editorial; comment]," *J Natl Cancer Inst*, vol. 88, pp. 779-81, 1996.
4. J. Kurhanewicz, D. B. Vigneron, H. Hricak, et al., "Three-dimensional H-1 MR spectroscopic imaging of the in situ human prostate with high (0.24-0.7-cm<sup>3</sup>) spatial resolution," *Radiology*, vol. 198, pp. 795-805, 1996.
5. J. Kurhanewicz, D. B. Vigneron, R. G. Males, et al., "The Prostate: Magnetic Resonance Imaging and Spectroscopy: Present and Future," in *Radiologic Clinics of North America*, H. Hricak and P. R. Carroll, Eds. New York, New York: W. B. Saunders Co., 2000, pp. 115-138.
6. T. Hara, N. Kosaka, N. Shinoura, et al., "PET imaging of brain tumor with [methyl-C11]choline," *J Nucl Med*, vol. 38, pp. 842-7, 1997.
7. N. Shinoura, M. Nishijima, T. Hara, et al., "Brain tumors: detection with C-11 choline PET," *Radiology*, vol. 202, pp. 497-503, 1997.
8. T. Hara, N. Kosaka, and H. Kishi, "PET imaging of prostate cancer using carbon-11-choline," *J Nucl Med*, vol. 39, pp. 990-5, 1998.
9. T. Hara, N. Kosaka, T. Kondo, et al., "Imaging of brain tumor, lung cancer, esophagus cancer, colon cancer, prostate cancer, and bladder cancer with [C-11]choline," *J Nucl Med*, vol. 38 (suppl), pp. 250P (abstract), 1997.
10. T. Hara, K. Inagaki, N. Kosaka, et al., "Sensitive detection of mediastinal lymph node metastasis of lung cancer with 11C-choline PET," *J Nucl Med*, vol. 41, pp. 1507-13, 2000.
11. I. J. Jong, T. H. Que, J. Pruim, et al., "Imaging of bladder cancer using carbon-11 choline positron emission tomography," *J. Nucl. Med.*, vol. 41 (5 Suppl), pp. 74, 2000.
12. J. Kotzerke, J. U. Prang, B. Neumaier, et al., "Carbon-11 choline positron emission tomography (PET) of prostate cancer -- first clinical experience," *J. Nucl. Med.*, vol. 41 (5 Suppl), pp. 74, 2000.
13. J. Kotzerke, J. Prang, B. Neumaier, et al., "Experience with carbon-11 choline positron emission tomography in prostate carcinoma," *Eur J Nucl Med*, vol. 27, pp. 1415-9, 2000.
14. T. R. Degrad, R. E. Coleman, S. W. Baldwin, et al., "Fluorine-18 fluorocholine (FCH) as an oncological PET tracer: evaluation in

- murine prostate cancer xenograft model," *J. Nucl. Med.*, vol. 41 (5 Suppl), pp. 231, 2000.
15. T. R. Degrado, R. E. Coleman, S. Wang, et al., "Synthesis and Evaluation of F18-labeled Choline as an Oncologic Tracer for Positron Emission Tomography: Initial Findings in Prostate Cancer," *Cancer Research*, vol. 61(1), pp. 110-117, 2001.
  16. J. S. Huber, S. E. Derenzo, J. Qi, et al., "Conceptual Design of a Compact Positron Tomograph for Prostate Imaging," *IEEE Trans Nucl Sci*, vol. NS-48, pp. 1506-1511, 2001.
  17. T. F. Budinger and G. T. Gullberg, "Three-dimensional reconstruction in nuclear medicine emission imaging," *IEEE Trans Nucl Sci*, vol. NS-21, pp. 2-20, 1974.

Figures:

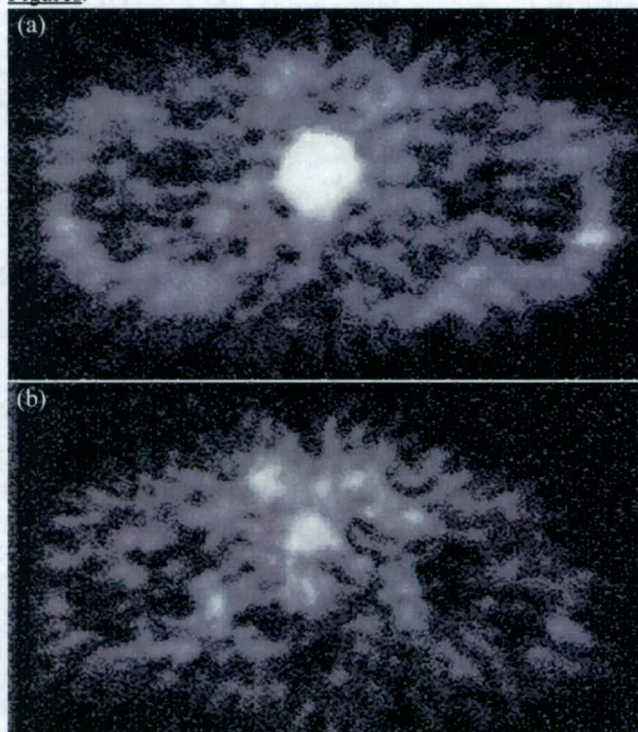


Fig. 1: [ $^{11}\text{C}$ ]choline image of prostate cancer (a) before and (b) after treatment. These grayscale images indicate a high (white) uptake in the prostate cancer compared with a low (gray) uptake elsewhere. Images are provided by Hara and co-workers [8].

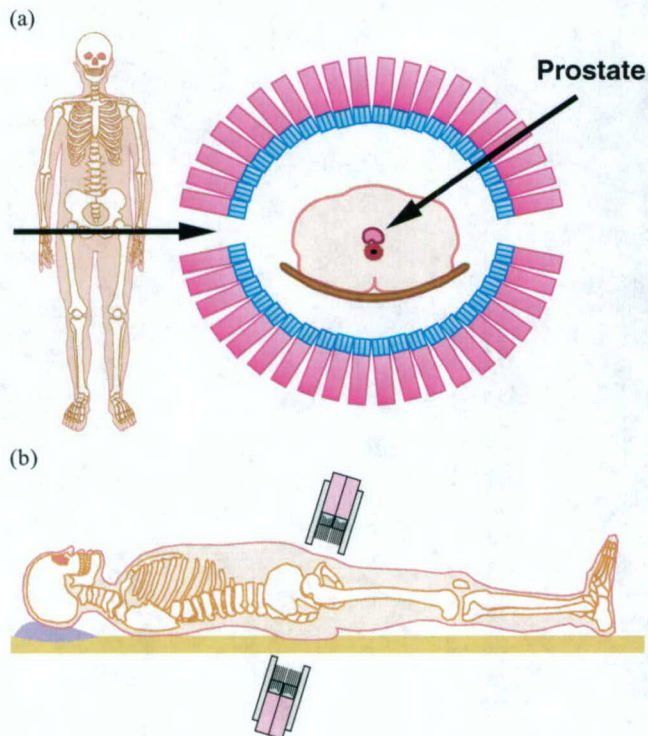


Fig. 2: Positron tomograph for prostate imaging. (a) Drawing of a transaxial view through prostate, showing the patient centered between two detector banks. The individual detector modules are angled to point towards the prostate. (b) Drawing of the sagittal view. The bottom arc is fixed below the patient bed, whereas the top arc adjusts vertically for patient access and compactness. Both detector banks are tilted and positioned as close as

possible to the prostate, which improves sensitivity and minimizes attenuation.

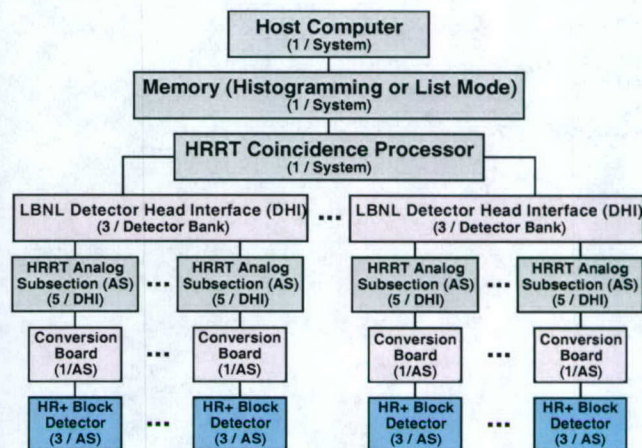


Fig. 3: Diagram of the complete data collection chain, showing the custom LBNL and CTI components and their inter-relations. The camera will use 80 CTI ECAT HR+ block detectors, 28 LBNL conversion boards, 28 CTI HRRT Analog Subsection boards, 6 LBNL custom Detector Head Interface boards, 1 CTI Coincidence Processor and a PC.

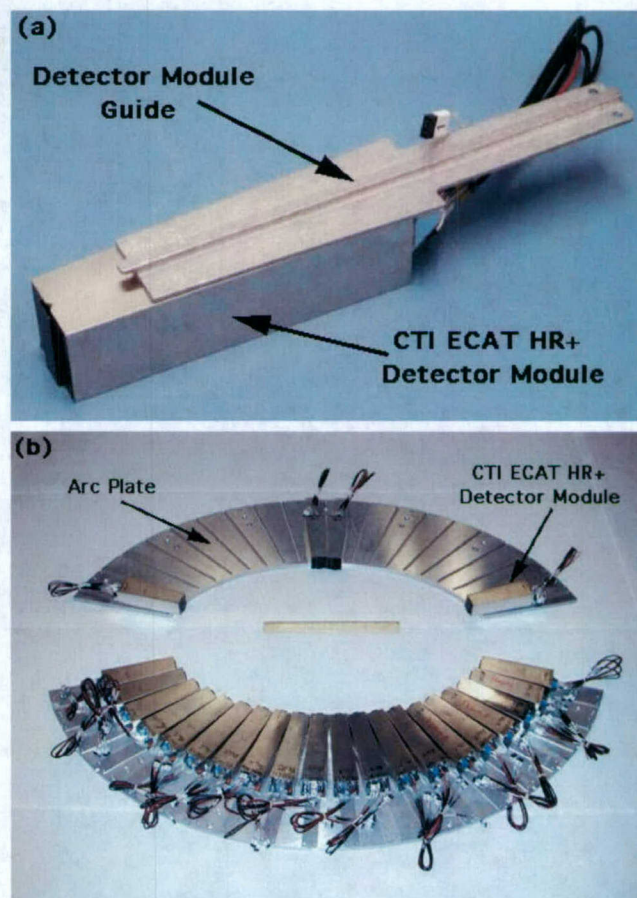


Fig. 4: (a) CTI ECAT HR+ detector module with an aluminum guide epoxied along its midline. (b) Photograph of the top and bottom aluminum arc plates with some of the CTI ECAT HR+ detector modules mounted in place. Each detector module has an aluminum guide that slides along a groove in the arc plate and is stopped (and secured against the arc plate) using a mortise and tenon. The detector modules are individually angled to point towards the center of the camera.

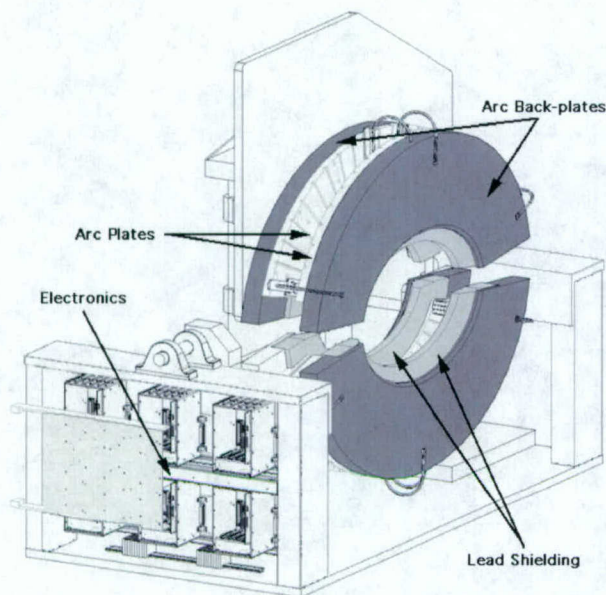


Fig. 5 3-D drawing of the prostate PET camera with some gantry details, as viewed from the side. Only a few detector modules are shown in place. The arc plates (with detector module grooves, shown in Fig. 4b) are mounted onto thicker aluminum arc back-plates that also hold the lead shielding in place. The arc plates (white), arc back-plates (dark gray) and lead shielding (light gray) are symmetric (~left and right in drawing) since there are two axial rows of detector modules. The upper bank is mounted onto a main aluminum back-plate in order to control the vertical motion using a hand-crank, allowing upward movement for patient access and downward to maximize sensitivity. A second hand-crank is used to adjust the overall tilt of both upper and lower banks. The near end of the drawing shows the electronics. The six DHI boards are mounted horizontally to the housings that hold their corresponding Analog Subsection boards. The Coincidence Processor board is mounted onto the cabinet door. The power supplies are mounted on the far end of the gantry. Most of the cabling is not shown, as well as the patient bed.

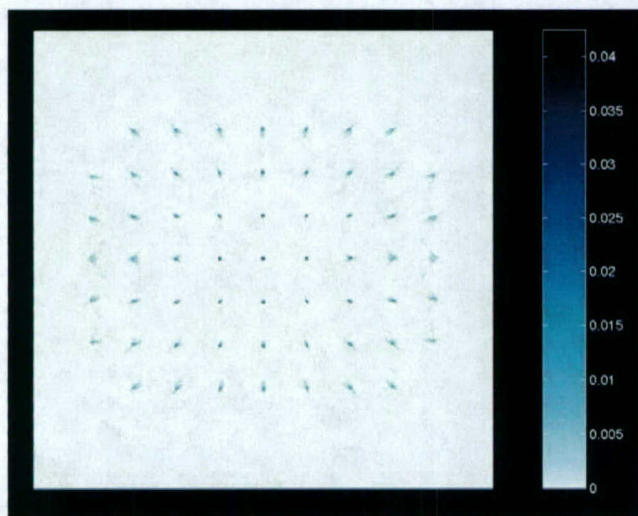


Fig. 6: Statistical noise-free reconstructed image of a point source grid when arcs are separated by the 'nominal' distance. The point sources are 5 cm apart, with the grid covering the majority of the field of view. Most point sources are located between pixels (*i.e.*, the center point source contributes to four nearby pixels). All point sources are visible (black = high uptake). Increased radial blurring is observed near the outer surface of the patient as expected due to penetration effects. However, good resolution is demonstrated in the center near the prostate, with minimal blurring in a 10 cm diameter central region. The central point has both a radial and tangential fwhm of 2 mm. The surrounding eight points have a

radial fwhm of 4 mm and tangential fwhm of 3 mm. Improved resolution is expected when the reconstruction corrects for detector penetration.

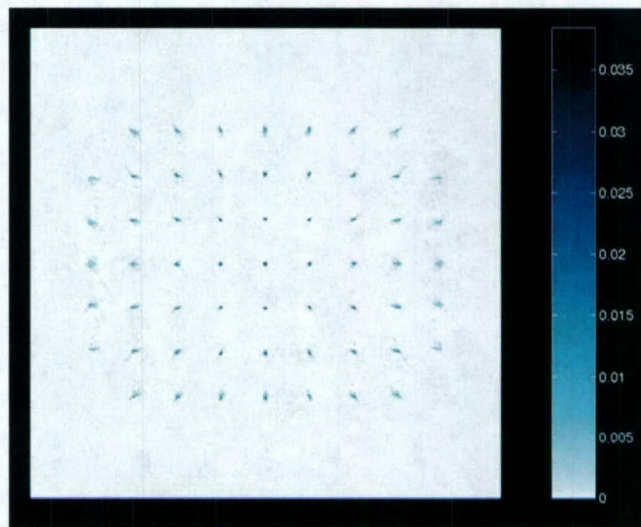


Fig. 7: Statistical noise-free reconstructed image of a point source grid when arc gap distance is increased by +5 cm from 'nominal' position. The point sources are 5 cm apart, with the grid covering the majority of the field of view. All point sources are clearly visible (black = high uptake). Good resolution is still demonstrated in the center near the prostate, with minimal blurring in a 10 cm diameter central region.

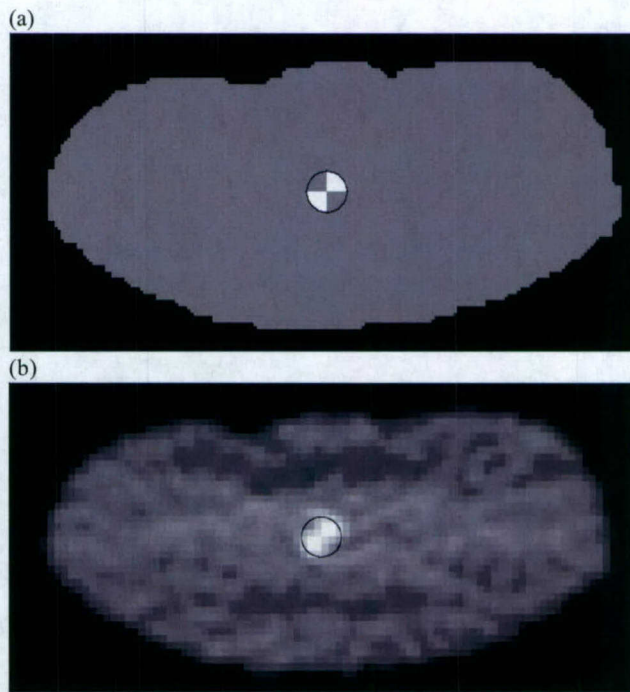


Fig. 8: (a) Body outline of patient with 2.5 cm diameter circular "prostate" divided into quadrants with "tumors" placed in the upper right and lower left quadrants (white = high uptake), assuming a tumor to background ratio of 2:1. The "patient" is 37.5 cm wide and 18.0 cm deep. (b) Reconstructed image of the phantom using an iterative maximum likelihood algorithm that assumes a 30% scatter fraction and 20% randoms fraction. Image represents 745 kcounts in a single slice, which should be achievable with a 6 minute scan after a 10 mCi injection. Both tumors are clearly visible.

# MAP Image Reconstruction for Arbitrary Geometry PET Systems with Application to a Prostate-Specific Scanner

Jicun Hu, Jinyi Qi, Jennifer S. Huber, William W. Moses and Ronald H. Huesman

**Abstract** — PET systems are usually constructed with multiple detector blocks composed by arrays of rectangular scintillation crystals, which function as the basic element for positron annihilation detection. Conventional PET scanners have a circular geometry with detector blocks uniformly placed on a ring. Recently, several PET systems with different geometries have been developed to meet specific applications. In this paper, we propose a method to obtain MAP reconstruction from arbitrary geometry PET systems. It is well known that precise modeling of the system matrix, which relies heavily on the scanner geometry, is the key to obtaining an accurate image reconstruction. In our reconstruction software, the scintillation crystals can be located at any position with any orientation so that arbitrary geometry PET systems can be accurately modeled. Each line of response is modeled using numerical calculation of the solid angle effect in coincidence detection and penetration effect of 511 keV photons through multiple detector blocks, while accounting properly for the gaps between them. No rebinning is used. This accurate modeling of geometric response and precise calculation of the penetration distance of the chord within crystals are the main advantages of the proposed reconstruction method. We implemented both an EM-type algorithm and a preconditioned conjugate gradient algorithm for image reconstruction. The method can handle both list mode and histogrammed data. We validate our method using Monte Carlo simulations and data collected from the prostate specific scanner developed at Lawrence Berkeley National Laboratory.

## I. INTRODUCTION

Positron emission tomography (PET) is an important modality for functional imaging. Most existing PET systems are composed of detector blocks, which are arrays of multiple rectangular scintillation crystals. Conventional PET scanners have a circular geometry with detector blocks uniformly placed on a ring. With the advances in instrumentation technology, various noncircular PET systems have been developed to meet specific practical applications. These systems include the parallel two-planar [1,2] and

rectangular positron emission mammography (PEM) [3] for breast imaging, hexagonal HRRT brain scanner [4], the dual-layer MADPET-II small animal scanner [5] and elliptical prostate-specific PET [6]. It is very likely that more PET systems of different geometries will be designed in the future. This presents a challenge for the image reconstruction software since it is usually based on specific geometries and has to be developed separately for different PET systems. In order to meet this challenge, we propose a generalized PET reconstruction method based on detector blocks.

In this work, we proposed a method that can reconstruct data collected from virtually any PET system as long as the software is provided with an input file accurately describing the geometry of the system - the size, location and orientation of all the detectors composing the camera. For computational efficiency, we first group scintillation crystals into detector blocks, and then group detector blocks into detector heads, which are rectangular arrays of detector blocks with the same orientation. Each detector head can have a flexible number of detector blocks and be located at any position with any orientation in the three-dimensional space, so that arbitrary PET systems can be modeled. For example, our rectangular PEM system is composed of four detector heads with each head facing the center of the field of view. In a single ring PET system, each head corresponds to a single detector block facing the center of the ring. In addition to the flexibility to model arbitrary PET systems, the proposed method also has the advantages of accurate geometrical registration of coincidence chords and the precise calculation of the penetration distance of the chord into crystals. We validate our method using Monte Carlo simulation and real data collected from a prostate-specific scanner [6], which has an elliptical geometry to maximize the tumor detection efficiency while reducing the cost.

## II. METHOD

PET data are modeled as a collection of independent Poisson random variables with the expectation  $\bar{y}$  related to the unknown image  $x$  by an affine transform

$$\bar{y} = Px + r + s \quad (1)$$

where  $P$  is the system matrix with the  $(i,j)$ th element containing the probability of detecting an event from voxel  $j$

---

Jicun Hu, Jennifer S. Huber, William W. Moses and Ronald H. Huesman are with the Department of Nuclear Medicine and Functional Imaging, Lawrence Berkeley National Laboratory, Berkeley, CA 94720

Jinyi Qi is with the Department of Biomedical Engineering, University of California, Davis, CA 95616 and the Department of Nuclear Medicine and Functional Imaging, Lawrence Berkeley National Laboratory, Berkeley, CA 94720

at the LOR  $i$ ,  $r$  and  $s$  account for the randoms and scatters. The system matrix  $P$  can be factorized as follows [7].

$$P = P_{\text{det.sens}} P_{\text{atten}} P_{\text{geom}} P_{\text{range}} \quad (2)$$

$P_{\text{range}}$  is an image domain blurring matrix that models the positron range effect. It is dependent on the radioisotope used in the clinical task. It is not included in the system matrix calculated in this work.

$P_{\text{geom}}$  models the geometric probability that a photon pair emitted from one voxel is detected by a detector pair, in the absence of attenuation and assuming perfect photon conlinearity and uniform detector efficiency. We used a numerical calculation that models both solid angle and crystal penetration effects in the coincidence detection.

$P_{\text{atten}}$  is a diagonal matrix containing the attenuation factors for each LOR. When an attenuation map is available, the attenuation effect can also be included into  $P_{\text{geom}}$  to model the variation of attenuation inside each LOR.

$P_{\text{det.sens}}$  is a diagonal matrix that contains normalization factors.

In this work, a MAP reconstruction is obtained by

$$\hat{x}(y) = \arg \max_{x \geq 0} [L(y|x) - \frac{\beta}{2} x R x'] \quad (3)$$

$$L(y|x) = \sum_i (y_i \log \bar{y}_i - \bar{y}_i - \log y_i!) \quad (4)$$

where  $y$  is the projection data,  $R$  is a positive definite (or semi-definite) matrix and  $\beta$  is the smoothing parameter that controls the resolution of the reconstructed image.

In order to obtain a good image reconstruction, each component in the system matrix represented by equation (2) has to be accurately calculated. In modeling the scanner geometry, the block structure, the orientation and location of the scintillation crystals, the gap between the detector blocks are the main concerns. In order to account for above concerns, we propose a method that can accurately calculate the projection matrix  $P_{\text{geom}}$  for arbitrary geometry PET scanners based on detector blocks.

The basic component of a PET camera is a scintillation crystal, whose size (length, width and height) and material are known. Multiple scintillation crystals compose a detector block and multiple detector blocks compose a detector head. Finally, a number of detector heads are placed at different locations with different orientations to compose a PET tomograph (Fig. 1). The block and detector head structure is purely for computation efficiency and does not reduce the generality of the reconstruction software.

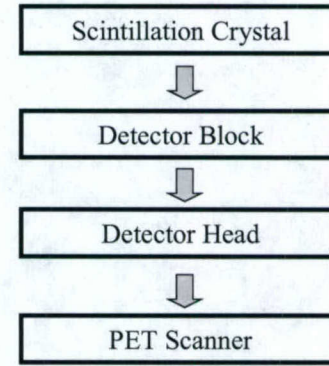


Fig. 1 Composition of a PET tomograph

Fig. 2 shows an illustration of the detector head, which is defined as a rectangular array of multiple detector blocks. A gap may exist between detector blocks along the axial and transaxial directions, and its effect is accounted for in the system matrix calculation.

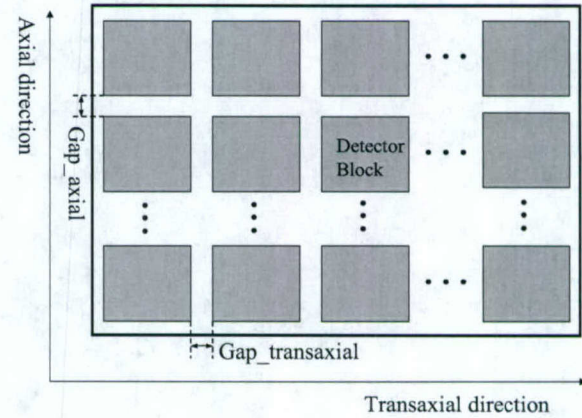


Figure.2 Illustration of a detector head

With the detector head defined as above, any PET tomograph can be composed by placing multiple detector heads at different positions with different orientations. This information can be completely described by an initialization file, which acts as an input file to the reconstruction code.

For a detector block, the following information is specified in the initialization file.

- Number of crystals in transaxial direction
- Number of crystals in the axial direction
- Number of depth levels in the crystal. Some detector modules have the capability to measure the depth of interaction [8].
- Size of the crystal in axial direction
- Size of the crystal in transaxial direction
- The length of the crystal

For a detector head, the following information is specified in the initialization file.

- Location of the head

- Orientation of the head
- Number of detector blocks in transaxial direction
- Number of detector blocks in axial direction
- The gap between detector blocks in transaxial direction
- The gap between detector blocks in axial direction

The software also allows the specification of the detector head pairs within which there is no coincidence detection.

The method we used to compute the system matrix can be either detector head driven for histogrammed data or event driven for list mode data. In both cases, we iterate through crystal pairs that detect coincidences. If the chord defined by the crystal pair intersects the image volume, then we calculate the distance the chord travels in each image voxel. Also the penetration distance of the chord into the crystals is calculated. The modeling of the physics of the data acquisition process for a crystal pair is similar to that in [9]. The probability of a coincidence from a voxel  $j$  detected by crystal pair  $k$  is defined as follows.

$$P_{k,j} = c \left( \frac{l_{kj} e^{-\mu(w_{1k} + w_{2k})} e^{-\int \mu_0(l) dl}}{r_k^2} \right) \quad (5)$$

where  $c$  is a constant,  $\mu$  is attenuation coefficient of the scintillation crystals.  $l_{kj}$  is the distance the chord  $k$  defined by crystal 1 and 2 travels within voxel  $j$ .  $\mu_0$  is the attenuation coefficient of the object to be imaged.  $r_k$  is the length of chord  $k$ .  $w_{1k}$  is the distance the chord travels through the crystals before interaction happens within crystal 1 and  $w_{2k}$  is the distance chord  $k$  travels through the crystals before interaction happens within crystal 2. One of the advantages of the proposed software is that  $w_{1k}$  and  $w_{2k}$  can be very accurately calculated, while accounting properly for the gap between detector blocks and the multiple layer structure in some PET systems. Fig. 3 shows how a chord may travel through multiple detector blocks before interaction. Fig. 3(a) shows a single layer system. Fig. 3(b) shows a dual-layer system that also measures interaction depth. In either case, we firstly search the detector modules which intersect the chord and calculate the attenuation of the chord within those modules. Here the chord is a line segment instead of an infinite line.

In order to account properly for the geometric response of each chord, we sub-divide each crystal into  $m \times n \times q$  smaller regions along each dimension and average the response over a large number of lines. Thus, each crystal pair  $k$  corresponds to  $(mnq)^2$  chords and equation (5) becomes:

$$P_{k,j} = c \sum_{i=1}^{(mnq)^2} \frac{l_{kij} e^{-\mu(w_{1ki} + w_{2ki})} e^{-\int \mu_0(l_i) dl_i}}{r_{ki}^2} \quad (6)$$

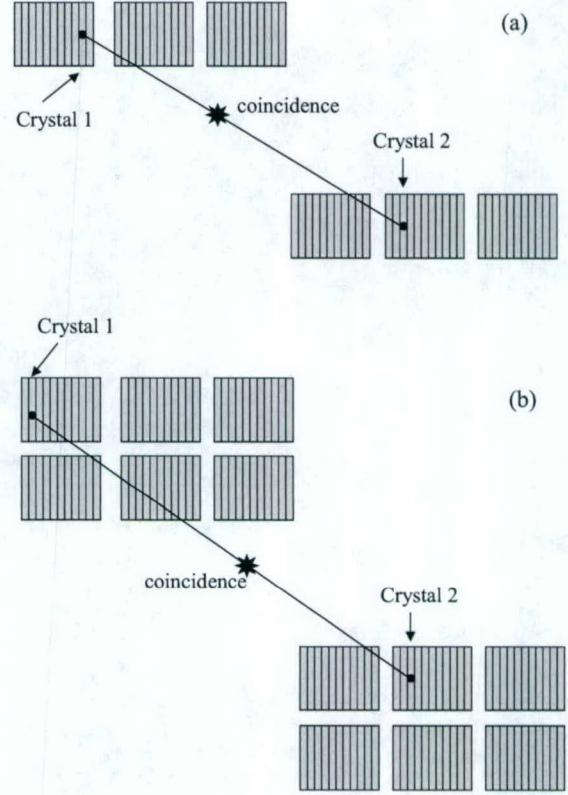


Fig. 3 Calculation of penetration distance into crystals for (a) a single layer system (b) a dual layer system

where  $k_i$  represents  $i$ th chord for crystal pair  $k$ .  $l_{kij}$  is the length of  $i$ th chord within voxel  $j$ .  $\int \mu_0(l_i) dl_i$  denotes the line integral of the source density over  $i$ th chord. The larger the values of  $(m,n,q)$  are, the more accurate the system model is.

From the information provided in the initialization file, the geometrical factors of detector heads, such as locations, orientations and the gap between the detector blocks or crystals, can be easily and accurately modeled. Therefore, the spatial location and orientation of all crystals which determine the coincidence chord in the PET tomograph can be precisely known. This is one of the main advantages of the proposed software.

### III. RESULTS

We applied the developed software to the prostate scanner developed at our laboratory, which has a very irregular geometry to maximize the prostate cancer detectability while minimizing cost. The proposed camera can achieve twice the detection efficiency as a conventional 2D PET camera with approximately one-quarter the detector costs.

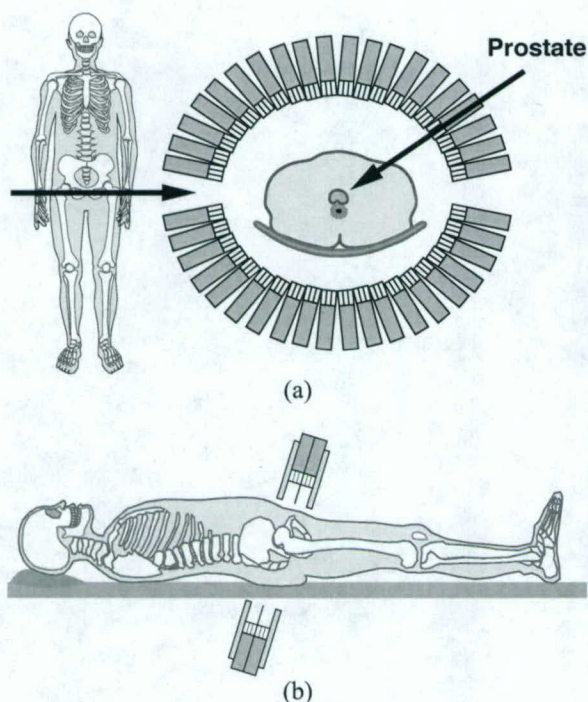


Fig. 4 (a) Transaxial view of the scanner  
(b) Sagittal views of the scanner

Fig. 4 shows the transaxial and sagittal views of the developed two-ring prostate camera design. The bottom bank is fixed below the patient bed, and the top bank moves upward for patient access and downward for maximum sensitivity. Each bank consists of 40 conventional block detectors such as those in the Siemens/CTI ECAT HR+ (8 x 8 array of 4.5 mm x 4.5 mm x 30 mm BGO crystals), forming two arcs with a minor axis of 44 cm and major axis of 60 cm with each detector block angling towards the camera center near the prostate location to reduce the penetration effect for photons emitted from prostate. The prostate camera has one-half the axial coverage and uses about one-fourth the number of detectors as in a conventional PET system. However, since the average distance to the detectors is approximately one-half that of a conventional 2D PET system, the solid angle for a central source is approximately double. Annihilation photons from other parts of the field of view (FOV) will suffer increased penetration effects, but these FOV regions are less important. Both detector banks can be tilted to image the prostate while minimizing attenuation.

#### Monte Carlo Simulation

Fig. 5(a) shows a reconstruction from the Monte Carlo simulated data representing 850k counts without adding any scattering and random. Fig. 5(b) shows a reconstruction from Monte Carlo simulated data (850k counts) with 50% scattering fraction. The white spot in the center simulates a prostate tumor whose diameter is 1 cm. The tumor to background activity ratio is 2:1. The voxel size in the reconstruction is  $0.45\text{cm}^3$ .

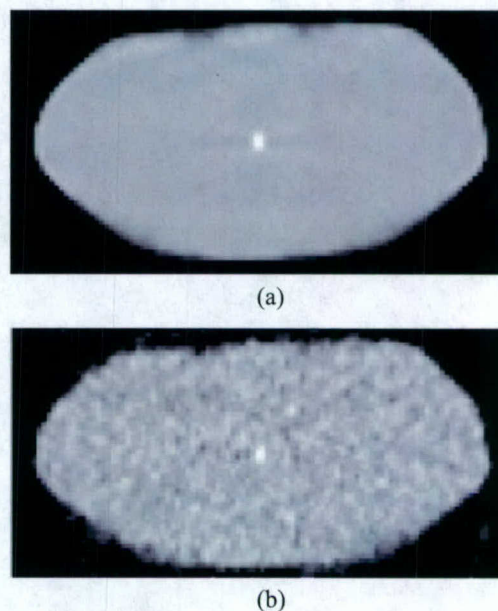


Fig. 5 Reconstructions from Monte Carlo simulations  
(a) No scattering and random added (b) Scattering added

#### Real Data

A 37 points and a co-centric cylinder phantom were scanned. Both phantoms were filled with  $^{18}\text{F}$ -water. The initial activity density for the 37-point phantom was  $30 \mu\text{Ci/ml}$  and 7 million counts were collected. The initial activity density for the co-centric cylinder phantom was  $0.4 \mu\text{Ci/ml}$  for the outside and  $1.2 \mu\text{Ci/ml}$  for the inside cylinder. 20 million counts were collected. Figure 6 shows the illustration (a) and reconstructed image (b) of the 37-point phantom. Figure 7 shows the illustration (a) and reconstruction (b) for the concentric-cylinder phantom with three times higher activity density in the inner cylinder than the outer cylinder. Random and attenuation are corrected for both reconstructions. In the read data reconstruction, data collected within the same detector bank are not included. The artifacts shown in the upper and lower portions of the reconstructed cylinder phantom are due to the incomplete data sampling. Since both phantoms are uniform axially, the images shown are reconstructions of 2D sinograms obtained by single-slice rebinning. However, the reconstruction software is intrinsically 3D.

#### IV. CONCLUSION AND DISCUSSION

An MAP reconstruction software, which can process both histogrammed and list mode data, has been developed for image reconstruction from arbitrary PET scanners constructed with scintillation crystals. The scanner geometry can be defined using an initialization file. The size of the detector block and detector head is flexible so that scintillation crystals can be placed in arbitrary locations in the 3D space. The proposed method can model the exact LOR location and its

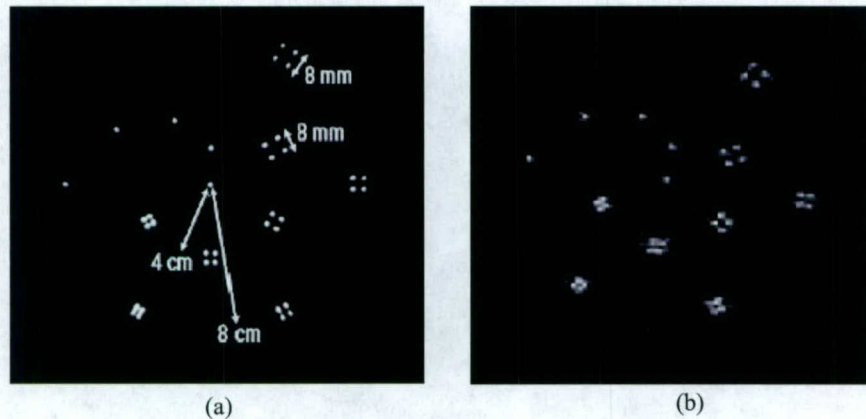


Fig. 6 Illustration (a) and reconstruction (b) of a 37 points phantom

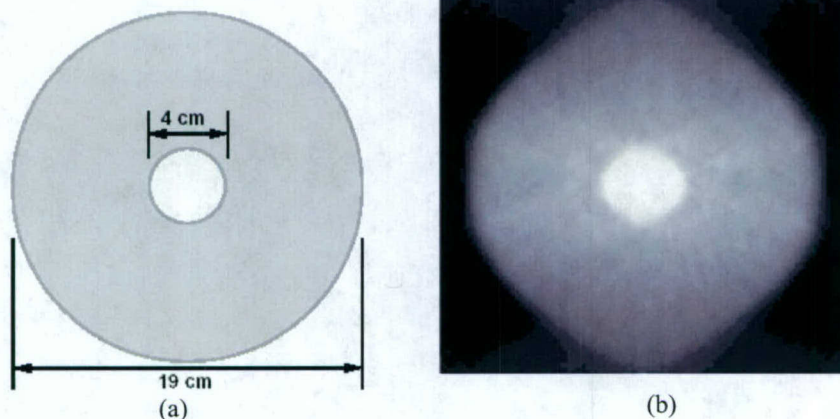


Fig. 7 Illustration (a) and reconstruction (b) of a co-centric cylinder phantom

geometric response, while accounting properly for the crystal penetration effect and the gap between detector modules. It can also handle LORs that pass through multiple detector blocks. This feature is important to those new PET scanners using multiple layers of detectors. We tested the reconstruction software using Monte Carlo simulations and the real data collected from the prostate scanner developed at our Laboratory and obtained very good results despite of the irregular sampling.

#### V. ACKNOWLEDGEMENTS

This work is supported in part by NIBIB grant no. R01 EB00194, DOD grant no. DAMD17-02-1-0081 and DOE contract no. DE-AC03-76SF00098.

#### VI. REFERENCES

1. C. Thompson, K. Murthy, Y. Picard, I.N. Weinberg and R. Mako, "Positron emission mammography(pem): A promising technique for detecting breast cancer". IEEE transactions on Nuclear Science, vol. 42 pp1012-1017, 1995
2. N. Doshi, Y. Shao, R. Silverman and S. Cherry. "Design and evaluation of a LSO PET detector for breast cancer imaging" Medical Physics, vol. 27, pp. 1535-1543, 2000
3. P. Virador, W. Moses, R. Huesman and J. Qi, "3D reconstruction in PET cameras with irregular sampling and depth of interaction," IEEE Transactions on Nuclear Science, vol. 48 pp. 1524-1529, 2001
4. M. Schmand, K. Wienhard, M. Casey, L. Eriksson, W.F. Jones, J.H. Reed, J. Treffer, M. Lenox, P. Luk, J. Bao, J.W. Young, K. Baker, S.D. Miller, C. Knoess, S. Vollmar, N. Richerzhagen, G. Flugge, W.D. Heiss and R. Nutt. "Performance evaluation of a new LSO high resolution research tomograph-HRRT," In proceedings of IEEE Nuclear Science Symposium and Medical Imaging Conference, Seattle, WA, 1999
5. D.P. McElroy, W. Pimpl, M. Djelassi; B.J. Pichler; M. Rafecas; T. Schuler; S.I. Ziegler, "First results from MADPET-II: a novel detector and readout system for high resolution small animal PET", IEEE Nuclear Science Symposium Conference Record, Vol. 3 pp. 2043 - 2047 2003
6. J. S. Huber, S. E. Derenzo, J. Qi, et al., "Conceptual Design of a Compact Positron Tomograph for Prostate Imaging," IEEE Trans Nucl Sci, vol. 48, pp. 1506-1511, 2001.
7. J. Qi, R. M. Leahy, S. R. Cherry, A. Chatzioannou and T. H. Farquhar., "High-resolution 3D Bayesian image reconstruction using the microPET small-animal scanner," Phys Med Biol, vol. 43, pp. 1001-13, 1998.
8. J. S. Huber, W. W. Moses, M. S. Andreaco, et al., "A LSO scintillator array for a PET detector module with depth of interaction measurement," IEEE Trans. Nucl. Sci., vol. 48, pp. 684-688, 2001
9. Huesman, R.H.; Klein, G.J.; Moses, W.W.; Jinyi Qi; Reutter, B.W.; Virador, P.R.G. "List-mode maximum-likelihood reconstruction applied to positron emission mammography (PEM) with irregular sampling" IEEE Transactions on Medical Imaging, vol. 19, pp. 532 - 537, 2000